

1 **1. Introduction**

2 Glass is largely used in practice as a structural material, e.g. as beam or plate elements able to carry the loads
3 deriving from other structural components or external forces. Especially in the field of façades and building
4 envelopes, the use of glass panels combined with steel frames, aluminum supporting bracings or cable-nets
5 resulted in an extremely wide variety of case studies. Typical applications of glass assemblies are often
6 derived – and properly modified, to account for the tensile brittle behavior of glass – from practice of
7 traditional construction materials (e.g. steel structures, sandwich structures, etc.), and take the form of
8 properly designed and well-calibrated mechanical or chemical connections (e.g. steel fasteners, silicone
9 sealant joints, adhesives, etc.) able to offer a certain structural interaction among multiple glass components.
10 Recent design trends, however, are often oriented towards the minimization of metal joints and mechanical
11 connectors. Typical examples consist in fact in frameless glazing systems, in which glass to glass interaction
12 is provided by sealant joints or adhesives only (Fig.1). This is the case of beam-like glass elements used in
13 practice as stiffeners for façade or roof plates, where the coupling between them is often provided by
14 continuous silicone joints. From a structural point of view, the effect of silicone joints can be compared to a
15 partially rigid shear connection, of which the effectiveness should be properly taken into account.

16 In [5], for example, results of a recent research study carried out on laterally restrained (LR) glass beams in
17 LTB have been presented. Assessment of existing analytical models available in literature for the prediction
18 of the Euler's critical buckling moment of LR beams under constant bending moment, accounting for the
19 shear stiffness provided by continuous, partially rigid lateral restraints, has been presented. Based on
20 extended finite-element (FE) linear bifurcation analyses (*lba*), the effects of various loading conditions of
21 practical interest (e.g. mid-span concentrated F or uniformly distributed loads q , applied both at the top or
22 bottom edge of the laterally restrained beams) have then been also emphasized. The final result consisted in
23 correction factors of practical use for a suitable prediction of the Euler's critical moment for LR glass beams
24 in LTB, thus in correction factors numerically calibrated to properly take into account the effects of silicone
25 joints, beam-to-joint stiffness ratios, loading condition.

26 In this work, based on earlier contributions [5, 6, 7], the LTB response of glass beams laterally restrained by
27 means of structural silicone joints is further assessed by means of incremental buckling, Finite-Element (FE)

1 numerical simulations. While several studies have been dedicated to the assessment of the LTB structural
2 behaviour of laterally unrestrained (LU) glass beams, and buckling design methods have also been proposed
3 (e.g. [8-11]), the extension of the same simplified analytical methods must be checked. At the same time,
4 although practical formulations are provided in [5] for the estimation of the Euler's critical moment of LR
5 glass beams under various loading conditions, it is well known that a proper assessment of the buckling
6 resistance of a given structural system should be carried out by means of more refined analyses able to
7 account for several mechanical and geometrical aspects.

8 For this purpose, small specimens of silicone joints are subjected to shear experiments, to properly estimate
9 their elastic stiffness, but also the ultimate resistance and deformation capacities, with respect to common
10 applications of practice. Incremental nonlinear analyses are then performed on a wide set of geometrical
11 configurations. The main advantage of these FE-investigations is given by the appropriate description of
12 effects deriving from initial curvatures (with specific shape and amplitude), as well as the detection of the
13 ultimate condition as the first attainment of tensile cracking in glass or failure of the silicone joint,
14 respectively. Based on extended parametric studies, a practical design method based on a suitable design
15 buckling curve is also proposed for the LTB verification of LR glass beams.

16

17 **2. Euler's critical moment of laterally restrained glass beams in LTB**

18 **2.1.Literature background for LR members in LTB**

19 LTB of structural beams with lateral restraints has been widely investigated and assessed in the last years. In
20 [12] and [13], research studies have been dedicated to the typical LTB response of doubly-symmetric steel I-
21 beams, with careful attention for possible distortional buckling phenomena in the steel webs. Khelil & Larue
22 proposed in [14, 15] a simple analytical model for the assessment of the critical buckling moment in steel-I
23 sections with LR tensioned flanges, highlighting that the presence of rigid continuous lateral restraints in
24 steel I-beams under LTB can have a weak influence, compared to their unrestrained Euler's critical buckling
25 moment. The same authors presented in [16] a further alternative, analytical approach for the LTB
26 assessment of I-beams continuously restrained along a flange by accounting for the buckling resistance of an
27 equivalent, isolated "T" profile. The latter approach, due to its basic assumptions, typically consisted in a

1 conservative analytical prediction for the LTB resistance of rigidly LR steel I-beams. Conversely, the main
2 advantage of this method consisted in the implementation of Appendix values of practical use for designers.
3 The LTB behaviour of thin-walled cold-formed steel channel members partially restrained by steel sheeting
4 has been assessed, under various boundary conditions, by Chu et al. [17], by means of an energy-based
5 analytical model. Bruins [18] numerically investigated the LTB response of steel I-section profiles under
6 various loading conditions (e.g. distributed load q , mid-span concentrated force F , constant bending moment
7 M_y) and laterally restrained by single, elastic, discrete connectors, highlighting through parametric FE-
8 numerical studies and earlier experiments that partial elastic restraints can have significant influence on the
9 overall LTB response. The effects deriving from initial geometrical curvatures with different shape were also
10 emphasized by means of FE simulations, while simple equations were proposed as strength design method
11 for ‘rigid’ discrete lateral restraints. Chu et al. [19] assessed by means of an energy-based method the
12 influence of lateral restraints on the LTB response of cold-formed steel zed-purlin beams under various
13 loading / boundary conditions, demonstrating that lateral restraints generally provide an increase of the
14 unrestrained critical load, but this improvement is largely affected by boundaries or the point of load
15 application. Further assessment of structural effects deriving from discrete rigid supports on the buckling
16 behaviour of steel beams and braced columns are discussed in [20-24].

17

18 **2.2. Glass beams under constant bending moment M_y**

19 Based on [5, 6, 7, 15], in this work the attention is focused on the global LTB behaviour and ultimate
20 buckling resistance of LR glass beams, rather than on their Euler’s critical moment only.

21 For this purpose, let us consider first the laterally unrestrained (LU) monolithic beam depicted in Fig. 2. The
22 beam, having a monolithic rectangular $b \times t$ cross section composed of glass (with E and G the Young’s
23 modulus and shear modulus respectively), is simply supported at the ends of its buckling length L_0 . Fork end-
24 restraints enable the occurring of out-of-plane deflections due to the applied positive (e.g. bottom edge in
25 tension) constant bending moment M_y .

26 When a continuous lateral restraint is introduced along its top edge (e.g. Fig. 3a) to provide a connection
27 between the glass beam and the supported panels, the structural interaction among them can be described in

1 the form of a partially rigid, continuous shear restraint with elastic stiffness per unit-of-length k_y and
2 rotational stiffness per unit-of-length k_θ (Fig. 3b).
3 From a practical point of view, as also discussed in [5], the problem described in Figs. 2-3 requires the
4 implementation of closed-form solutions of suitable use. However, the presence of continuous elastic,
5 partially rigid, lateral restraints typically leads to rather complex analytical models, often able to provide
6 closed-form solutions for simple loading / boundary conditions only, hence suggesting the implementation of
7 computationally expensive FE-models for further detailed studies. With reference to Figs. 2 and 3,
8 specifically, the elastic LTB behaviour of LR glass beams can be rationally described by means of the
9 analytical model proposed by Larue et al. in [15]. It was also shown in [5] that its Euler's critical buckling
10 moment $M_{cr,R}^{(E)}$ can in fact be calculated, with "R" the subscript denoting the presence of lateral restraints, as
11 (with $k_\theta \approx 0$ the rotational stiffness):

$$12 \quad M_{cr,R}^{(E)} = z_M k_y \left(\frac{L_0}{n_R \pi} \right)^2 + \sqrt{\left[EJ_z \left(\frac{n_R \pi}{L_0} \right)^2 + k_y \left(\frac{L_0}{n_R \pi} \right)^2 \right] \left[GJ_t + z_M^2 k_y \left(\frac{L_0}{n_R \pi} \right)^2 \right]}. \quad (1)$$

13 where $n_R \geq 1$ is an integer representative of the number of half-sine waves able to minimize Eq.(1).
14 In the same equation, J_t is the torsional moment of inertia ($J_t \approx bt^3/3$ when $b/t > 6$); $J_z = bt^2/12$ signifies the
15 moment of inertia about the minor z -axis; M_y is the applied bending moment; z_M is the distance between the
16 lateral restraint and the x -axis, while v and θ_x denote the vertical deflection of the beam (z -direction) and the
17 rotation of the cross-section about the x -axis.

18 It is thus expected, mainly based on the elastic shear stiffnesses k_y provided by the adopted continuous joints,
19 that the estimated critical moment $M_{cr,R}^{(E)}$ will be higher than the Euler's critical load $M_{cr}^{(E)}$ of the same LU
20 beam geometry. In the latter case, in fact, the beam would be able to offer a maximum LTB theoretical
21 resistance equal to:

$$22 \quad M_{cr}^{(E)} = M_{cr} = \frac{n\pi}{L_0} \sqrt{EJ_z GJ_t} = \frac{\pi}{L_0} \sqrt{EJ_z GJ_t}, \quad (2)$$

23 with $n=1$ is the integer value able to minimize – independently on the geometrical and mechanical properties
24 of the investigated beams – the predicted critical moment $M_{cr}^{(E)}$.

1 The structural benefit provided by continuous lateral restraints, specifically, could be rationally quantified in
 2 the form of a magnifying coefficient R_M able to give (for $0 < k_y < \infty$):

$$3 \quad M_{cr,R}^{(E)} = R_M M_{cr}^{(E)}, \quad (3)$$

4 with $M_{cr}^{(E)}$ given by Eq.(2) and $R_M = f(k_y, b, t, L_0, z_M, n_R)$ accounting for the effects deriving from the joint
 5 shear rigidity k_y , the beam aspect ratio, glass elastic stiffnesses, as well as the position of the applied elastic
 6 restraints (z_M) or the number n_R of half sine waves able to minimize, based on Eq.(1), the predicted critical
 7 buckling moment $M_{cr,R}^{(E)}$.

8 When $z_M = b/2$ (Fig. 3), for example, Eq.(3) leads to:

$$9 \quad R_M = \frac{6bL_0^3k_y + \sqrt{(3b^2L_0^2k_y + 16n_R^2Ebt^3)(12L_0^4k_y + 97.4n_R^4Ebt^3)}}{39.5n_R^2bt^3E}, \quad (4)$$

10 where $E = 70\text{GPa}$ and $G \approx 0.41E$ for glass [25].

11 Differing from the case of a LU beam (Eq.(2)), where the minimum critical moment $M_{cr}^{(E)}$ strictly depends
 12 on $n=1$, it is important to notice that this is not the case of LR beams with a partially rigid connection, where
 13 an integer value $n_R \neq 1$ could be identified as the critical one able to minimize Eq.(1), due to a combination of
 14 mechanical and geometrical aspects such as the beam slenderness ratio, the joint stiffness, the beam-to-joint
 15 stiffness ratio, etc. Based on the k_y stiffness of the adopted lateral restraint, moreover, the critical buckling
 16 moment $M_{cr,R}^{(E)}$ given by Eq.(1) for a same beam geometry can largely vary. Examples are shown in Fig.4,
 17 where the amplification factor given by Eq.(4) for a monolithic glass beam ($L_0 = 3000\text{mm}$, $b = 300\text{mm}$, $t =$
 18 10mm) is proposed for various shear stiffnesses k_y ($10^{-4} \text{N/mm}^2 \leq 500 \text{N/mm}^2$). As demonstrated also in [5],
 19 the actual Euler's critical moment $M_{cr,R}^{(E)}$, that is the absolute minimum R_M amplification factor, is given by
 20 the lower envelope of R_M plots obtained by changing the number of half sine waves n_R .

21 In the same figure, the typical shear stiffness contribution k_y , expected from silicone joints is also emphasized
 22 (dotted area), where $\approx 0.184\text{N/mm}^2 \leq k_y \leq \approx 0.6136\text{N/mm}^2$ per unit-of-length values correspond to the range
 23 of elastic stiffnesses offered by common structural sealants available in commerce for glass [5, 27, 29, 30].

1 Maximum structural benefits deriving from application of continuous silicone joints in glass beams in LTB is
2 also emphasized in Fig.5, in the form of a magnifying factor R_M proposed as a function of various
3 thicknesses t for beams with $b= 100\text{mm}$ and $L_0= 1000\text{mm}$ or $L_0= 5000\text{mm}$, respectively. The collected R_M
4 values, specifically, are derived from Eq.(4) as the minimum envelope of the analytical estimations obtained
5 for each beam geometry (t, b, L_0) and joint stiffness (k_y).

6

7 **2.3.Preliminary FE-numerical validation**

8 FE-models were also developed with the computer software ABAQUS/Standard [26], to verify the accuracy
9 of Eq.(5) and to investigate the global LTB behavior of glass beams laterally restrained by means of
10 continuous silicone joints. Linear bifurcation analyses (*lba*) were carried out on a wide range of geometrical
11 properties, with continuous lateral restraints characterized by a sufficiently extended set of shear stiffnesses
12 k_y . The critical buckling moment $M_{cr,R}^{(E)}$ of each beam subjected to a constant and positive bending moment
13 M_y was numerically predicted and compared to the corresponding analytical estimation (Eq.(4)).
14 Accordingly, the correspondence between the numerical and analytical number of half sine-waves n_R
15 associated to the lowest critical moment was checked. The typical FE-model consisted of S4R 4-node,
16 quadrilateral, stress/displacement shell elements with reduced integration and large-strain formulation (type
17 S4R of ABAQUS element library; Fig. 6). Glass was described as an isotropic, indefinitely linear elastic
18 material ($E= 70\text{GPa}$, $\nu= 0.23$ [25]). A refined and regular mesh pattern was used, with l_{mesh} the characteristic
19 size of quadrilateral shell elements comprised between 3mm and 15mm, depending on the $b \times L_0$ dimensions
20 of the studied beams.

21 To take into account the presence of continuous, partially rigid lateral restraints, a series of indefinitely linear
22 elastic springs directly connected to a rigid substructure and characterized each one in terms of elastic
23 stiffness K_y , was introduced along the top edge of each beam ($z_M= b/2$, Fig. 6). The elastic stiffness K_y , being
24 dependent on l_{mesh} , was in fact estimated as $K_y= k_y \times l_{mesh}$ ($K_y= k_y \times 0.5 l_{mesh}$ for the two springs close to the
25 beam end sections), with $10^{-4} \text{ N/mm}^2 \leq k_y \leq 10^4 \text{ N/mm}^2$ the range of elastic stiffnesses taken into account
26 throughout this exploratory parametric study. Loads and boundaries for the simply supported, fork-end
27 restrained beams in LTB were finally introduced in each FE-model by means of bending moments M_y

1 applied at the barycentric node of the end sections, as well as nodal translational and rotational restraints
2 for the same cross-sectional nodes. These modeling assumptions, rather in agreement with earlier studies
3 related to the LTB response of laterally restrained structural members (e.g. [19]) were then accounted for a
4 numerical and analytical study extended to a sufficiently wide range of key parameters ($6\text{mm} \leq t \leq 19\text{mm}$;
5 $100\text{mm} \leq b \leq 300\text{mm}$, $1000\text{mm} \leq L_0 \leq 5000\text{mm}$). Comparative examples are proposed in Fig.7, where the
6 rather good agreement between numerically and analytically predicted R_M amplification factors is
7 emphasized for three selected geometrical configurations, by changing the joint shear stiffness k_y . Extended
8 *lba* simulations presented in [5] highlighted that in general Eq.(4) provides fairly accurate predictions for the
9 LTB critical moment of glass beams restrained by silicone joints. Parametric calculations also resulted in an
10 average percentage discrepancy Δ_{RM} , with:

$$11 \quad \Delta_{RM} = 100 \frac{(R_M)_{Eq.(5)} - (R_M)_{ABAQUS}}{(R_M)_{ABAQUS}} \quad (5)$$

12 A maximum discrepancy equal to $\approx \pm 0.5\%$ was found for joint shear stiffnesses per unit of-length k_y of
13 practical interest for continuous sealant restraints (e.g. $\approx 0.184 \text{ N/mm}^2 \leq k_y \leq \approx 0.6136 \text{ N/mm}^2$).

14 As expected, major effects of different joint stiffnesses k_y manifested not only in a significant increase of the
15 R_M coefficient for the examined beams, thus of their theoretical critical buckling moment $M_{cr,R}^{(E)}$, but also in
16 a substantial modification of their reference buckling shape (e.g. critical n_R value), thus in a variation of their
17 global LTB response. In this sense, a detailed incremental buckling investigation should be performed by
18 taking into account the actual critical buckling shape for each geometrical configuration, with $u_{0,max} = L_0/400$
19 the recommended amplitude [33].

20 Parametric studies highlighted an almost exact correlation between the analytical and numerical number of
21 half sine-waves n_R associated to comparative data collected in Fig.7, especially in presence of lateral
22 restraints able to provide a buckling strength increase up to ≈ 10 times the unrestrained beams (e.g. $1 \leq R_M \leq$
23 10 , with $1 \leq n_R \leq 8-10$ depending on the beam geometry). Some examples are proposed in Fig.8 for some
24 beam geometries and joint stiffnesses of practical interest for this study.

1 A partial lack of correlation between analytical and numerical half sine-waves n_R able to provide the lowest
 2 critical buckling moment for the studied beams was found only in presence of stiff continuous lateral
 3 restraints ($10 \text{ N/mm}^2 \leq k_y \leq 10^2 \text{ N/mm}^2$ and $\approx 10 \leq n_R \leq \approx 18$, in this investigation), not of primary interest for
 4 this study.

5
6

7 **2.4. Glass beams under uniformly distributed load or concentrated load at mid-span**

8 While for LR glass beams under constant bending moment M_y it was shown that closed-form solutions of
 9 literature can provide a rational prediction of their theoretical LTB resistance (both in terms of Euler's
 10 critical load and fundamental buckling shape (e.g. n_R)), the same approach cannot be directly applied to other
 11 loading conditions. This is the case for example of beams in LTB under distributed loads q or mid-span
 12 concentrated loads F . Although for LU beams in LTB it is reasonable to estimate the maximum effects
 13 deriving from q or F loads applied to their barycentric axis (e.g. point G of Fig.9) by accounting for an
 14 equivalent bending moment

$$15 \quad M_y \equiv M_{y,eq} = \frac{M_{y,max}}{k_1}, \quad (6)$$

16 with:

17 k_1 a correction factor depending on the distribution of the applied loads (Table 1), and

18 $M_{y,max}$ the maximum bending moment due to the applied q or F loads respectively, that is

$$19 \quad M_{y,max} = qL_0^2/8 \text{ or } M_{y,max} = FL_0/4;$$

20 the same simplified method cannot be used for LR beams, due to the presence of partially rigid, continuous
 21 lateral restraints able to modify the global LTB behavior of the examined beams. At the same time,
 22 according to practical applications of glass beams and fins in roofs and façades, it is rationally expected an
 23 eccentric application of q and F loads (e.g. $e_{load} \neq 0$, with $e_{load} \equiv z_M = +b/2$ denoting top-edge loads (point A
 24 of Fig.9) and $e_{load} \equiv -z_M = -b/2$ signifying bottom-edge loads (point B of Fig.9)) will further affect the
 25 theoretical LTB resistance of the studied systems.

1 Exploratory FE-studies confirmed, for example, that the mentioned loading conditions can strongly modify
 2 the predicted Euler's critical load, as well as result in a critical number of half sine waves n_R not directly
 3 comparable to the solution derived in presence of M_y moments.

4 In terms of magnifying factor R_M obtained for same beam geometry, for example, interesting numerical
 5 comparisons are collected in Fig.10 for the same beam geometry under (a) top-edge or (b) bottom edge
 6 distributed q or mid-span F loads, respectively. In these plots, specifically, the R_M amplification factor is
 7 separately calculated for the q or F loading conditions – in accordance with Eq.(5) – as the ratio between the
 8 numerical critical buckling moment $M_{cr,R}$ (ABAQUS-*lba*) of each LR beam and the corresponding LU
 9 critical moment M_{cr} ($R_M \geq 1$), being

$$10 \quad \left(M_{cr,R}^{(E)} \right)_F = \left(F_{cr,R}^{(E)} \right)_{ABAQUS-eb} \frac{L_0}{4} \quad (7)$$

11 and

$$12 \quad \left(M_{cr,R}^{(E)} \right)_q = \left(q_{cr,R}^{(E)} \right)_{ABAQUS-eb} \frac{L_0^2}{8}. \quad (8)$$

13 As also discussed in [5], the application of top-edge distributed loads (q^A) typically results – almost
 14 independently on the beams' aspect ratio – in numerical predictions generally comparable to those deriving
 15 from constant moments M_y . Major discrepancy was conversely found for the same beam geometries and joint
 16 stiffnesses k_y under the action of top-edge mid-span loads (F^A). The latter condition generally resulted in non-
 17 conservative predictions for the examined LR beams, independently on the load eccentricity e_{load} from the
 18 beams' longitudinal axis. A comparable general LTB behavior was then observed also for LR beams under
 19 bottom-edge mid-span loads F , typically manifesting in limited number of half sine-waves n_R (e.g. Fig.11).

20 From a practical point of view, approximate or closed-form solutions for the estimation of the LTB
 21 theoretical buckling resistance of LR glass beams under various loading conditions (e.g. Eq.(6) and Table 1)
 22 would certainly represent a suitable method for designers. However, the correction factor k_l mentioned in
 23 Eq.(6) should be properly calculated, since strictly related to the joint stiffness k_y , the number of half sine
 24 waves n_R associated to each loading condition, etc.

1 In this context, it should be noticed that wide series of parametric numerical simulations (ABAQUS-*lba*)
 2 discussed in [5] generally provided predictions well agreeing with plots collected in Fig.10. As a result,
 3 numerically calibrated correction factors k_I^* associated to various beam geometries and loading conditions,
 4 but well defined joint shear stiffness (0.184N/mm^2 [7]), were estimated as:

$$5 \quad k_I^* = f(k_y, e_{load}) = \frac{\left(M_{cr,R}^{(E)}\right)_i}{M_{cr,R}^{(E)}} = \frac{\left(M_{cr,R}^{(E)}\right)_i}{R_M M_{cr}^{(E)}}, \quad (9)$$

6 where $\left(M_{cr,R}^{(E)}\right)_i$ signifies the Euler's critical moment derived from Eqs.(7)-(8), depending on the examined
 7 loading condition, while $M_{cr,R}^{(E)}$ is obtained from Eq.(3) – for a same beam geometry and joint stiffness, with
 8 $M_{cr}^{(E)}$ and R_M respectively defined in Eqs.(2)-(3) – under constant bending moments M_y .

9 Results collected in Figs.12 and 13 for LR beams under top-edge or bottom-edge q or F loads, respectively,
 10 with $8\text{mm} \leq t \leq 25\text{mm}$ the nominal thickness and $1000\text{mm} \leq L_0 \leq 5000\text{mm}$ the buckling length, are proposed
 11 in the form of k_I^* correction factors (Eq.(9)) as a function of the beams L_0/b ratios. As expected, the so
 12 obtained correction factors k_I^* manifested partial sensitivity to the beams geometrical properties and
 13 torsional stiffness GJ_t (e.g. higher dispersion of k_I^* values for beams with small L_0/b ratios). In any case, an
 14 almost stable LTB behaviour was found throughout the parametric study, for each loading condition.

15 In the same Figures, for this reason, minimum values $k_{I,min}^*$ are also highlighted, since an approximate but
 16 conservative prediction of the theoretical Euler's critical moment for the studied LR beams could be
 17 performed as:

$$18 \quad \left(M_{cr,R}^{(E)}\right)_i = \left(k_{I,min}^*\right) \times \left(R_M M_{cr}^{(E)}\right), \quad (10)$$

19 with:

20 i denoting the specific loading condition (top-edge or bottom-edge q or F loads),

21 $\left(M_{cr,R}^{(E)}\right)_i$ given by Eqs.(7)-(8)

22 $M_{cr}^{(E)}$ and R_M defined in Eqs.(2)-(3), and

23 $\left(k_{I,min}^*\right)_i$ signifying the corresponding minimum correction factor for each i loading condition

24 (Figs.12-13 or Table 2).

1
2
3
4
5
6
7
8
9
10
11
12
13
14
15
16
17
18
19
20
21
22
23
24
25
26

3. Experimental calibration of the constitutive mechanical behavior of structural sealant joints

Based on the LTB background discussed in Section 2, further studies were focused on the mechanical characterization of the constitutive behavior of structural sealant joints of common use in glass practice. While the estimation of the theoretical Euler’s critical load for a LR glass beam in LTB, based on Eqs.(1) and (10), would require as input parameter the elastic shear stiffness k_y on the adopted sealant joints, refined buckling investigations should be able to properly take into account the full stress-strain behavior of joints up to failure. Differing from LU glass beams, where the buckling failure mechanism could result from the limited glass tensile strength only, the effective LTB resistance of LR glass beams should be in fact assessed by correctly taking into account the structural contribution of silicone joints – e.g. increased critical buckling load $M_{cr,R}^{(E)}$ and a number of half sine-waves n_R – but also the possible failure mechanisms occurring in the joints themselves, together with glass tensile cracking. As a result, the elastic shear stiffness k_y would not represent an exhaustive information for the development of more refined studies.

3.1. Specimens and test methods

Shear tests were performed at Ghent University [6, 7] and ten experiments, equally divided in two series (A and B), were carried out on small specimens of silicone sealant joints. The chosen material was Dow Corning® 895 (DC 895) [27], a one-component sealant used in practice for glass structures. Based on the producer recommendations, structural sealant joints made with DC 895 should have a width w_{sil} (e.g. the joint dimension in the direction of shear loading) determined by structural and thermal calculations, but in any case comprised between $w_{sil,min}= 6\text{mm}$ and $w_{sil,max}= 15\text{mm}$.

Based on these assumptions, each specimen – well representative of a small part of a continuous elastic sealant joint - consisted of a sample with total length $l_{sil}= 100\text{mm}$. The difference between specimens of series A and B was then given by the $w_{sil} \times h_{sil}$ cross-sectional dimensions of each joint, respectively equal to $w_{sil}= h_{sil}= 6\text{mm}$ (series A) and $w_{sil}= h_{sil}= 15\text{mm}$ (series B). An appropriate steel device was used to position the specimens and connect them to the loading machine. Prior to the execution of experiments, proper and

1 complete curing of the silicone was ensured systematically by means of extra specimens, prepared for this
2 purpose together with the shear test specimens.

3 The typical test setup for shear experiments is depicted in Fig. 14. Displacement-controlled tests were carried
4 out at 23° C, and a constant speed deformation of 5mm/min, as recommended by ETAG 002 [26], was
5 ensured during the experiments. While the top edge of the metal device was kept fixed and rigidly connected
6 to the loading machine, the bottom end of the steel device was subjected to a linearly increasing vertical load
7 F , up to failure of the specimens. The corresponding displacement u was continuously monitored during each
8 test.

9

10 **3.2. Test results**

11 Experiments generally resulted in a uniform response of specimens and in a similar pre-destructive behavior,
12 for both the series of specimens. Exemplificative images showing the progressive damage and failure of a
13 specimen are proposed in Fig.15. Based on the obtained test results, it was also found that in general the
14 elastic load F -displacement u response of specimens under shear loads can be rationally described in the
15 form of a straight line (Fig.16).

16 Based on test measurements, the average elastic stiffness per unit-of-length k_y was equal to 0.184N/mm², as
17 also highlighted in [5]. The tested specimens also highlighted an almost stable behavior, attaining large
18 displacements before failure, with an ultimate elongation $\varepsilon_u \approx (d_u - w_{sil})/w_{sil}$ equal to $\approx 416\%$ and $\approx 406\%$ for
19 series A and B respectively, with d_u denoting the maximum attained displacement. The obtained average
20 ultimate elongation $\varepsilon_{u,avg} \approx 411\%$ resulted well comparable to the nominal values of structural silicone
21 sealants available in commerce, being their maximum elongation at failure typically comprised between
22 $\varepsilon_{u,nom} \approx 400\%$ and $\varepsilon_{u,nom} \approx 600\%$ [27, 29, 30]. In terms of ultimate shear/tensile stress $\sigma_{u,avg}$, this parameter was
23 derived from experimental measurements as the average ratio between the failure load F_u of each series of
24 specimens and the corresponding resisting area A_{sil} , hence resulting in $\sigma_{u,avg} = 0.94 \text{ N/mm}^2$. Also in this latter
25 case, the calculated strength was in rather good agreement with the nominal ultimate tensile resistances of
26 common structural sealants ($\sigma_{u,nom} = 1.06 \text{ N/mm}^2$ [29] and $\sigma_{u,nom} = 1.2 \text{ N/mm}^2$ [30]).

27

4. Refined FE-parametric numerical study: incremental nonlinear analyses

4.1. General solving approach

In accordance with the mechanical properties of silicone specimens derived from experiments discussed in Section 3, further extended parametric investigations were carried out by means of additional FE-models derived from Section 2.

As known, *lba* simulations provide rather poor information, compared to static incremental nonlinear (*inl*) analyses, since they only provide the theoretical buckling resistance of a given structural system. A proper estimation of the effective LTB strength of the same beams discussed in Section 2, should in fact properly take into account that the expected failure load $M_{cr,R}^{(E)}$ could be strongly affected by several aspects, such as the effects of possible initial geometrical imperfections (with specific shape and amplitude), the premature tensile cracking of glass as well as possible failure mechanisms in the silicone joints, if subjected to large strains and tensile stresses exceeding their ultimate values ($\varepsilon_{u,avg}$, $\sigma_{u,avg}$). Further *inl* analyses were thus performed (static Riks procedure) on a selected set of geometrical configurations, based on FE-models derived from Section 2 (Fig.6) and properly modified.

4.2. Reference configuration and detection of the LTB failure condition

The axial springs representative of the sealant joints were characterized by means of the average shear stiffness $k_y = 0.184 \text{ N/mm}^2$ derived from the experiments (Section 2). The indefinitely linear elastic constitutive behavior of the same axial springs was otherwise characterized in terms of ultimate elongation $\varepsilon_u \equiv \varepsilon_{u,avg}$ and ultimate tensile stress $\sigma_u \equiv \sigma_{u,avg}$ (and σ_u properly related, in all the FE-models, to the mesh size l_{mesh} (e.g. area of influence of each spring) adopted for each LR beam) taken from Section 3. A brittle failure mechanism was also assigned to each axial spring, so that during each *inl* simulation, based on the assigned k_y , σ_u and ε_u mechanical parameters, the single connector could fail and be released at the first attainment of the $(\sigma_u, \varepsilon_u)$ ultimate condition. The examined glass beams were then assumed composed of different glass types (annealed (AN), heat strengthened (HS) and fully tempered (FT), respectively), characterized each one by isotropic linear elastic behavior ($E = 70 \text{ GPa}$, $\nu = 0.23$) and specific nominal characteristic tensile resistance

1 ($\sigma_{Rk,AN}= 45\text{MPa}$, $\sigma_{Rk,HS}= 70\text{MPa}$, $\sigma_{Rk,FT}= 120\text{MPa}$ respectively, based on [25]). Possible tensile cracking of
 2 glass, in this sense, was manually checked by continuously monitoring the maximum envelope of tensile
 3 stresses along the $L_0 \times b$ surface of each beam. Careful attention was finally paid for possible initial
 4 geometrical imperfections. Based on preliminary *lba* simulations carried out on the same beams, *inl* analyses
 5 were in fact performed on “deformed” reference configurations obtained as scaled buckling shapes having a
 6 specific number of half sine-waves n_R and a maximum amplitude $u_{0,max}$ along the beam length L_0 .

7

8 **4.3. Discussion of numerical results**

9 **4.3.1. LR beams under constant bending moment M_y**

10 Examples are proposed in Figs.17, 18 and 19 for the $L_0= 3000\text{mm} \times b=300\text{mm} \times t=10\text{mm}$ beam previously
 11 investigated, subjected to positive constant bending moments M_y . In them, the sensitivity of numerical
 12 buckling predictions to the shape (n_R) and maximum amplitude $u_{0,max}$ of initial geometrical imperfections, as
 13 well as to the effects of a possible failure in the silicone joints and a premature tensile cracking of glass
 14 ($\sigma_{max} \geq \sigma_{Rk}$) are highlighted.

15 In Fig.17, specifically, the maximum envelope of out-of-plane displacements u_{max} are proposed as a function
 16 of the R_M amplification factor for the same LU beam or restrained by means of continuous silicone joints
 17 (LR). For both the beams, the maximum amplitude of the initial geometrical imperfection is set equal to
 18 $u_{0,max}= L_0/400$, being the corresponding *lba* buckling shapes obtained performed on both the FE-models (with
 19 $n= 1$ a – as conventionally done for the buckling analysis of unrestrained beams – and $n_R= 4$ for the LU and
 20 LR beams respectively). As shown, preliminary neglecting possible cracking mechanisms in glass (and
 21 damage in the silicone joint, when present), the LU beam would ideally carry on a maximum bending
 22 moment asymptotically tending towards the theoretical critical buckling moment $M_{cr}^{(E)}$ given by Eq.(2) (e.g.
 23 $R_M \rightarrow 1$ for the LU beam). The laterally restrained beam (LR), otherwise, would be able to offer a
 24 significantly higher buckling resistance, e.g. up to ≈ 5.7 times the LU geometry, almost comparable to the
 25 corresponding theoretical critical buckling moment (Fig.17, $M_{cr,R}^{(E)} \cong 5.70M_{cr}^{(E)}$).

1 However, in the same Figure it is also possible to notice that for the LR beam both possible failure
 2 mechanisms occurring in glass or in the silicone joint would result in marked decrease of its ideal LTB
 3 resistance. By assuming in the same beam an indefinitely linear elastic mechanical behavior for glass, for
 4 example, the LTB failure mechanism would be governed by the progressive collapse of few axial connectors,
 5 representative of the silicon joint, typically resulting in an ultimate failure load significantly lower than the
 6 theoretical $M_{cr,R}^{(E)}$ value (point A of Fig.17, $R_M= 4.22$). Due to the separate failure of these connectors along
 7 the beam buckling length L_0 , in conjunction with the typical elastic LTB deformed shape of the examined LR
 8 beam (e.g. n_R), the post-cracked LTB response would also be characterized by an unsymmetrical deformed
 9 configuration (path AB of Fig.17).

10 In Fig.18, the R_σ stress ratio is also proposed for the silicone joint of the LR beam presented in Fig.17, where
 11 R_σ denotes the ratio between the measured stress σ_{max} in each axial connector and the corresponding ultimate
 12 resistance σ_u . Results are shown, along the beam buckling length x/L_0 (with $0 \leq x \leq L_0$), as a function of the
 13 applied bending moment (e.g. specific RM loading configuration derived from Fig.17). As shown, due to the
 14 assumed geometrical configuration for the examined LR beam ($n_R= 4$), damage in the axial connectors (e.g.
 15 $R_\sigma= \pm 1$) first occurs where the beam undergoes the maximum out-of-plane deflections. In the same Figure it
 16 is also possible to notice that – according to Fig.17 – that the ultimate LTB resistance of the examined LR
 17 beam would be clearly affected by the limited tensile resistance of glass. Depending on the type of glass and
 18 the corresponding characteristic tensile strength σ_{Rk} , the LTB collapse would occur due to premature glass
 19 failure (with AN, HS, FT in Figs.17-18 denoting the attainment of the tensile resistance for AN, HS and FT
 20 glass types, respectively). It is interesting to notice, in this context, that almost the same buckling collapse
 21 mechanism was found for all the beam geometries taken into account in this parametric investigation, and the
 22 failure of the silicone joints, accordingly, typically occurred for higher bending loads only. However, a
 23 detailed LTB investigation should necessarily take into account both the possible collapse mechanisms, for a
 24 given LR beam, since strictly related to several mechanical and geometrical influencing parameters.

25 Further related examples are shown for the same beam geometry in Fig.19, where again the *inl* numerical
 26 predictions are proposed as the maximum envelope of transversal displacements ($u_{max} - u_{0,max}$), as a function

1 of the corresponding R_M coefficient. Fig.19, specifically, emphasizes that the assumption of improper
2 buckling shapes for the description of possible initial geometrical imperfections for the examined LR beams
3 would typically result in a marked overestimation of their initial stiffness against out-of-plane deformations
4 and in an unrealistic overall LTB ultimate resistance (e.g. points B and AN, HS, FT of Fig.19). In addition
5 (buckling shape at point B of Fig.19), the inaccurate description of possible initial deviations from
6 straightness would result in the progressive – but inappropriate – modification of the overall deformed shape
7 and in the variation – due to the increase of the applied bending moments M_y – of the number of half-sine
8 waves n_R leading the beam to failure.
9 Certainly, apart from the shape assumed for the description of initial curvatures – the maximum amplitude
10 $u_{0,max}$ of geometrical deformations would also significantly affect the predicted buckling failure loads, as for
11 example shown in Fig.20. The difference between the proposed curves is given, for a same beam geometry,
12 joint shear stiffness k_y and loading condition (M_y), by the amplitude $u_{0,max}$ of the “reference” critical buckling
13 configuration (e.g. $n_R=4$). In the same Figure, the points A, B, C and AN, HS, FT signify the “LTB failure
14 configuration”, for each LR beam, due to collapse in the silicone joint or to the attainment of maximum
15 tensile stresses exceeding the corresponding resistance values, respectively. In this work, according to [31],
16 the reference maximum amplitude $u_{0,max}=L_0/400$ was kept reasonably constant throughout the parametric
17 FE-numerical study.

18

19 **4.3.2. LR beams under various loading conditions**

20 Application to the examined LR beams of different loading distributions (e.g. top-edge or bottom-edge q and
21 F loads) also manifested, as expected from *lba* exploratory investigations carried out in Section 2, in further
22 modification of the predicted overall LTB response of the same LR beams.

23 An example is shown in Fig.21 for a fixed LR geometry under bottom-edge (F^B) mid-span loads. Due to the
24 specific loading case, and based on a preliminary ABAQUS-*lba* simulation, the *inl* analysis is carried out on
25 a FE-model affected by an initial curvature shape well agreeing with Fig.11, with $u_{0,max}=L_0/400$. Results are
26 proposed in the form of the R_M amplification factor versus the maximum relative out-of-plane deflection
27 ($u_{max} - u_{0,max}$). In the same Figure, numerical predictions derived from Fig.17 for the same LR beam

1 geometry under constant bending moment M_y , are also recalled, to emphasize the effect of various loading
2 distributions. As shown, the implemented load eccentricity e_{load} (with $e_{load} = -z_M$ for the F^B case), typically
3 resulted in an appreciable LTB strengthening contribution (point B of Fig.21), compared to the same beam
4 geometry under constant moment M_y . However, also in this case glass tensile cracking would represent the
5 first condition of failure (points AN, HS, FT of Fig.21). Major effects deriving from the specific application
6 of loads were found not only in terms of maximum R_M amplification factors expected from each
7 configuration, but also in modification of the initial elastic stiffness for the investigated beams, as well as in
8 partially different distribution and increase of maximum tensile stresses and out-of-plane deformations in the
9 LR glass beams.

11 **5. Standardized LTB design method for glass beams with partially rigid lateral restraint**

12 **5.1. General approach**

13 According to analytical, numerical and experimental results presented in this paper, it was shown that
14 structural silicone joints can generally strongly modify the LTB response of glass beams, both in terms of
15 expected theoretical Euler's critical load and fundamental buckling shape, as well as in terms of overall load
16 vs. out-of-plane displacement response.

17 For practical purposes, in this context, a suitable design buckling approach for LR glass beams in LTB
18 should be able to correctly take into account the beam slenderness ratio and sensitivity to initial
19 imperfections, as well as the beam-to-joint stiffness ratio and its effects on the overall buckling response. At
20 the same time, a suitable design method should be able to properly take into account in the estimation of the
21 design buckling resistance, the effects deriving from both the brittle failure of glass in tension, as well as
22 possible collapse in the structural silicone joints. In this sense, parametric studies discussed in Section 4
23 highlighted – for the range of silicone joint and glass beam mechanical and geometrical properties examined
24 in this study – that the LTB collapse of continuously laterally restrained beams is strictly related to tensile
25 cracking of glass, rather than to possible failure in the silicone joints. However, the effects of these structural
26 joints on the expected overall buckling response should be carefully estimated, for design purposes.

1 For the verification of LU glass beams in LTB, practical design buckling curves developed in agreement
 2 with the Eurocode standard for steel structures [32] were for example proposed in [33]. For a given glass
 3 beam geometry (L_0 , b , t), glass type (e.g. σ_{Rk}) with continuous silicone joints ($z_M = b/2$, k_y) a suitable design
 4 procedure could require for example the satisfaction of the condition:

$$5 \quad M_{Ed} \leq M_{b,Rd}, \quad (11)$$

6 with $M_{Ed} \equiv M_y$ signifying the design equivalent bending moment and $M_{b,Rd}$ denoting the design buckling
 7 resistance. In [33], for example, it was proposed to calculate $M_{b,Rd}$ as:

$$8 \quad M_{b,Rd} = \chi_{LT} M_{Rd}, \quad (12)$$

9 with

$$10 \quad M_{Rd} = W_y \sigma_{Rd} \quad (13)$$

$$11 \quad W_y = b^2 t / 6 \quad (14)$$

12 the elastic resistant modulus; $\sigma_{Rd} = \sigma_{Rk} / \gamma_M$ the design tensile resistance of glass and γ_M a partial safety factor
 13 (the value $\gamma_M = 1.4$ was suggested in [33]).

14 In Eq.(12), moreover:

$$15 \quad \chi_{LT} = \frac{1}{\phi_{LT} + \sqrt{\phi_{LT}^2 - \bar{\lambda}_{LT}^2}}, \quad \text{for } \chi_{LT} \leq 1 \quad (15)$$

16 is a buckling reduction factor for beams in LTB, where:

$$17 \quad \phi_{LT} = 0.5 \left[1 + \alpha_{imp} (\bar{\lambda}_{LT} - \alpha_0) + \bar{\lambda}_{LT}^2 \right] \quad (16)$$

18 and

$$19 \quad \bar{\lambda}_{LT} = \sqrt{W_y \sigma_{Rk} / M_{cr}^{(E)}} \quad (17)$$

20 The coefficients α_{imp} and α_0 mentioned in Eq.(16) are representative of possible initial imperfections. Based
 21 on the assessment to experimental LTB results available in literature as well as on FE-numerical
 22 investigations, the values $\alpha_{imp} = 0.45$ and $\alpha_0 = 0.20$ were proposed in [33] for the verification of LU glass

1 beams affected by initial sine-shaped imperfections with maximum amplitude $u_{0,max}= L_0/400$ and subjected to
 2 constant bending moments M_y , mid-span concentrated loads F or uniformly distributed loads q .

3 In Eq.(17), moreover, $M_{cr}^{(E)}$ signifies the Euler's critical load given by Eq.(3) for LU beams.

4

5 **5.2.LTB design procedure for LR glass beams under constant bending moment M_y**

6 In this work, to assess the possible extension of the LTB design curve proposed in [33] for LU beams, further
 7 extended FE-investigations were carried out, as partly discussed in Section 4.

8 Monolithic glass beams with various geometrical properties (buckling length $L_0= 1000\text{mm}-5000\text{mm}$, with
 9 step increment of 500mm between each series of beams; height $b= 100\text{m}, 200\text{mm}, 300\text{mm}$; nominal
 10 thickness $t= 6\text{mm}, 8\text{mm}, 10\text{mm}, 12\text{mm}, 15\text{mm}, 19\text{mm}$) and glass types (AN, HS, FT) – opportunely
 11 combined with each other – were analyzed. Each beam, subjected to a constant, positive bending moment
 12 $M_{Ed} \equiv M_y$, was assumed affected by an initial geometrical imperfection of maximum amplitude $u_{0,max}= L_0/400$,
 13 obtained as the scaled critical buckling shape for each configuration (ABAQUS-*lba*). Continuous silicone
 14 joints were also characterized as discussed in Section 3, and shear stiffness values k_y were assumed
 15 comprised between $k_y= 0.184 \text{ N/mm}^2$ (average experimental value, Section 3) and $k_y= 0.6136 \text{ N/mm}^2$
 16 (maximum nominal value derived from [29, 30]).

17 As partially discussed in Section 4, for all the examined beams the failure condition was identified as the
 18 lower condition due to (i) glass tensile failure and (ii) collapse of the silicone joint, thus the failure bending
 19 moments M_u^* where separately collected for each FE-simulation. Numerical predictions are collected in
 20 Fig.22, where normalized FE-results are expressed in the form $(\chi_{LT}^*, \bar{\lambda}_{LT}^*)$ and compared to the design LTB
 21 curve proposed in [33] ($\alpha_{imp}= 0.45, \alpha_0= 0.20$), being:

$$22 \quad \chi_{LT}^* = \frac{M_u^*}{W_y \sigma_{Rk}}, \quad (18)$$

$$23 \quad \bar{\lambda}_{LT}^* = \sqrt{W_y \sigma_{Rk} / M_{cr,R}^{(E)}}, \quad (19)$$

24 with $M_{cr,R}^{(E)}$ the minimum critical buckling moment obtained from Eq.(1).

1 As shown, an interesting agreement between the LTB design curve calibrated in [33] and the ultimate
2 buckling resistance of laterally restrained beams was found. Compared to LU beams, the primary effect of
3 additional continuous lateral restraints, due to increased stiffness and overall resistance, typically results in a
4 decrease of the normalized slenderness ratio $\bar{\lambda}_{LT}$ (Eq.(19)) and an increase of the maximum load carrying
5 capacity, hence providing an increase of the buckling coefficient χ_{LT} . Numerical predictions collected in
6 Fig.22, specifically, have limited slenderness ratios $\bar{\lambda}_{LT}$ ($\approx 0.2 \leq \bar{\lambda}_{LT} \leq \approx 1.2$) due to the adopted sealant
7 joints. The same LU beam geometries, otherwise, would be characterized by higher slenderness values,
8 typically up to $\bar{\lambda}_{LT} \approx 2-2.5$. Maximum structural benefits deriving from continuous silicone joints, in this
9 context, were found for beams with small b/L_0 ratios. However, appreciable structural efficiency was
10 generally obtained for all the examined beams, as for example shown in Fig.23 ($L_0= 3000\text{mm}$, $b= 300\text{mm}$, $t=$
11 10mm ; AN glass; $k_y= 0.184 \text{ N/mm}^2$). In conclusion, based on extended assessment and validation of methods
12 discussed in this paper, it is expected that the LTB verification of glass beams subjected to constant bending
13 moments M_y and laterally restrained by means of continuous structural silicone joints could be performed by
14 means of Eq.(11), with χ_{LT} given by Eq.(15) and $\bar{\lambda}_{LT}$ given by Eq.(19).

15

16 **5.3.LTB design procedure for LR glass beams under uniformly distributed q or mid-span F loads**

17 In agreement with the extended studies partly discussed in previous Sections for the LTB response of LR
18 glass beams under uniformly distributed loads q or mid-span concentrated loads F , it is expected that the
19 same design buckling curve presented in Section 5.2 for beams under constant bending moments M_y could
20 provide rational predictions.

21 Examples are shown in Fig.24 for a beam under top-edge mid-span loads F^A ($L_0= 3000\text{mm}$, $b= 300\text{mm}$, $t=$
22 10mm ; AN glass; $k_y= 0.184 \text{ N/mm}^2$). Data are collected in the form $(\chi_{LT}, \bar{\lambda}_{LT})$ for the same geometry
23 laterally unrestrained (LU) or restrained by means of a continuous silicone joint (LR). In the latter case, the
24 non-dimensional parameters $(\chi_{LT}, \bar{\lambda}_{LT})$ are calculated according to Eqs.(18)-(19), based on ABAQUS-*lba*
25 (e.g. equivalent Euler's critical moment) and ABAQUS-*inl* (e.g. equivalent ultimate bending moment M_u)

1 predictions. From a practical point of view, based on the proposed comparisons, it is clear that the presented
2 LTB design buckling curve could be used for the verification of LR beams under various loading conditions.
3 The LTB verification, specifically, could be in fact carried out by means of Eq.(11), by simply calculating
4 the corresponding slenderness ratio $\bar{\lambda}_{LT}$ (Eq.(17)) deriving from the equivalent Euler's critical moment
5 $M_{cr,R}^{(E)}$ obtained from Eq.(10).

6 In Fig.24, specifically, it can be seen both for a LU and LR beam geometry that a full FE-numerical
7 calculation of the corresponding $(\chi_{LT}, \bar{\lambda}_{LT})$ parameters would provide close agreement with the
8 corresponding analytical predictions. The LU and LR dots, specifically, are in fact calculated in accordance
9 with Eqs.(18) and (19), that is by means of preliminary buckling analysis (for the estimation of the
10 equivalent Euler's critical moment $M_{cr,R}^{(E)}$ of Eq.(19)) and successive *inl*-analyses (for the calculation of
11 the equivalent failure moment M_u^* , as specified in Eq.(18)). The LU and LR dots are compared in Fig.24
12 with LU^* and LR^* points, respectively. In the case of the unrestrained beam (LU^*), the corresponding $(\chi_{LT},$
13 $\bar{\lambda}_{LT})$ parameters are calculated by means of Eqs.(15) and (19), with $M_{cr,R}^{(E)}$ derived from Eq.(10), by
14 assuming $R_M=1$ and $k_I=1.32$ (Table 1). For the LR^* point, conversely, the buckling coefficient χ_{LT} is given
15 again by Eq.(15), while the corresponding normalized slenderness ratio $\bar{\lambda}_{LT}$ (Eq.(19)) is analytically
16 calculated by taking into account the equivalent Euler's critical moment $M_{cr,R}^{(E)}$ provided by Eqs.(10), with
17 $k_{I,min}^*=0.75$ (Table 2) and RM derived from Eq.(4).

18 As shown, the proposed method and assumptions for LR beams under various loading conditions (e.g.
19 correction factors listed in Table 2), would result in a conservative but rather acceptable prediction for the
20 examined geometry, compared to a full FE-numerical calculation, hence confirming the general validity of
21 the proposed approach.

22

23

24

6. Summary and conclusions

In this paper, results of a recent research activity on the LTB behaviour of beam-like glass elements with continuous lateral restraints have been discussed. Depending on combinations of silicone joint stiffnesses and beam geometrical properties, analytical and FE-numerical calculations highlighted that their critical buckling moment can be strongly increased, especially in the case of slender beams.

However, the Euler's critical moment yields poor information only on the actual LTB ultimate resistance of laterally restrained (LR) glass beams, and detailed incremental analyses should be generally carried out to properly assess the effects of multiple mechanical and geometrical aspects (e.g. beam-to-joint stiffness ratio, failure mechanisms in glass or joints, initial geometrical imperfections, loading condition, etc.).

For this purpose, refined incremental nonlinear FE-analyses were performed on a large number of glass beams, to properly assess their global LTB response up to failure. Specifically, parametric analyses were carried out to take into account the effects of possible geometrical imperfections – both in terms of maximum amplitude and reference shape – as well as the premature buckling failure deriving from glass cracking in tension, or the occurring of possible failure mechanisms in the structural silicone joints. Simulations generally confirmed the appreciable efficiency of structural silicone joints, compared to laterally unrestrained (LU) beams, and highlighted – although in presence of continuous lateral supports – that their ultimate buckling resistance is strictly related to failure of glass in tension. Further studies were then extended to LR glass beams in LTB, by taking into account the effects of various loading conditions (e.g. top-edge or bottom-edge uniformly distributed q or mid-span concentrated loads F). Based on earlier contributions of literature, finally, a design LTB curve recently calibrated for the verification of LU glass beams has been recalled and applied to LR beams.

As shown, a rather good agreement was found, hence suggesting its possible extension for the design and verification of the studied structural typology. Certainly, further improvements of the current method could be derived from experimental and refined FE-investigations able to account for the structural interaction between the studied glass beams and the supported glass roof/plates. However, it is expected that discussed comparisons and methods could provide useful background and suitable tools for practical applications.

1 **References**

- 2 [1] www.dupont.com
- 3 [2] <http://www.spgintercitynews.ch/rachat-du-batiment-merck-serono-une-belle-victoire-pour-spg-intercity/>
- 4 [3] <http://natralight.co.uk>
- 5 [4] <http://malishevwilson.com>
- 6 [5] Bedon C, Amadio C (2015). Analytical and numerical assessment of the strengthening effect of
7 structural sealant joints for the prediction of the LTB critical moment in laterally restrained glass beams.
8 *Materials & Structures*, under review.
- 9 [6] Verhoeven E (2008). Effect van constructieve kitvoegen op de stabiliteit van glazen liggers (in Dutch).
10 Master thesis, LMO – Laboratory for Research on Structural Models, Ghent University.
- 11 [7] Belis J, Bedon C (2014). Strengthening effect of structural sealants on the LTB behaviour of glass
12 beams. Proceedings of Challenging Glass 4 & COST Action TU0905 Final Conference, EPFL Lausanne,
13 6&7 February.
- 14 [8] Belis J, Van Impe R, Lagae G, Vanlaere W (2003). Enhancement of the buckling strength of glass beams
15 by means of lateral restraints. *Structural Engineering and Mechanics*, 15(5): 495-511.
- 16 [9] Luible A (2004). Stabilität von Tragelementen aus Glas. Dissertation, EPFL Lausanne, Thèse 3014.
- 17 [10] Belis J (2005). Kipsterkte van monolithische en gelamineerde glazen liggers. Ghent: Ghent
18 University.
- 19 [11] Belis J, Bedon C, Louter C, Amadio C, Van Impe R (2013). Experimental and analytical assessment
20 of lateral torsional buckling of laminated glass beams. *Engineering Structures*, 51: 295-305.
- 21 [12] Kalkan I, Buyukkaragoz A (2012). A numerical and analytical study on distortional buckling of
22 doubly-symmetric steel I-beams. *Journal of Constructional Steel Research* 70: 289-297.
- 23 [13] Vrcelj Z, Bradford MA (2006). Elastic distortional buckling of continuously restrained I-section
24 beam-columns. *Journal of Constructional Steel Research* 62: 223-230.
- 25 [14] Khelil A, Larue B (2008). Simple solutions for the flexural-torsional buckling of laterally restrained
26 I-beams. *Engineering Structures* 30: 2923-2934.

- 1 [15] Larue B, Khelil A, Gueury M (2006). Elastic flexural-torsional buckling of steel beams with rigid
2 and continuous lateral restraints. *Journal of Constructional Steel Research* 63: 692-708.
- 3 [16] Larue B, Khelil A, Gueury M (2007). Evaluation of the lateral-torsional buckling of an I beam
4 section continuously restrained along a flange by studying the buckling of an isolated equivalent profile.
5 *Thin-Walled Structures* 45: 77-95.
- 6 [17] Chu X-T, Kettle R, Li L-Y (2004). Lateral-torsional buckling analysis of partial-laterally restrained
7 thin-walled channel-section beams. *Journal of Constructional Steel Research* 60: 1159-1175.
- 8 [18] Bruins RHJ (2007). Lateral-torsional buckling of laterally restrained steel beams. Report nr A-2007-
9 7, Technische Universiteit Eindhoven.
- 10 [19] Chu X-T, Rickard J, Li L-Y (2005). Influence of lateral restraints on lateral-torsional buckling of
11 cold-formed steel purlins. *Thin-Walled Structures* 43: 800-810.
- 12 [20] Taras A, Greiner R (2008). Torsional and flexural torsional buckling – A study on laterally restrained
13 I-sections. *Journal of Constructional Steel Research* 64: 725-731.
- 14 [21] Bradford MA (2000). Strength of compact steelbeams with partial restraint. *Journal of*
15 *Constructional Steel Research* 53: 183-200.
- 16 [22] Bradford MA (1998). Inelastic buckling of I-beams with continuous elastic tension flange restraint.
17 *Journal of Constructional Steel Research* 48: 63-77.
- 18 [23] Zhang L, Tong GS (2011). Lateral buckling of eccentrically braced RHS columns. *Thin-Walled*
19 *Structures* 49: 1452-1459.
- 20 [24] Nguyen CT, Joo HS, Moon J, Lee HE (2012). Flexural-torsional buckling strength of I-girders with
21 discrete torsional braces under various loading conditions. *Engineering Structures* 36: 337-350.
- 22 [25] EN 572-2:2004. Glass in buildings – Basic soda lime silicate glass products. CEN.
- 23 [26] Simulia (2009), ABAQUS v.6.9 Computer Software and Online Documentation, Dassault Systèmes.
- 24 [27] Dow Corning (2011). Product Information Dow Corning 895, Structural Glazing Sealant, one-part
25 silicone rubber.
- 26 [28] EOTA (1999). ETAG 002, Guideline for European technical approval for structural sealant glazing
27 systems (SSGS) – part 1: Supported and unsupported systems.

- 1 [29] Henkel (2012). Pattex SL 690 Solyplast - Structural Glass.
- 2 [30] Bostik (2008). V-70 High Streight Structural Glazing Silicone Adhesive Sealant – Technical Data
3 Sheet.
- 4 [31] Belis J, Mocibob D, Luible A, Vandebroek M (2011). On the size and shape of initial out-of-plane
5 curvatures in structural glass components. *Constr Build Mater*;25(5):2700–13.
- 6 [32] UNI-EN 1993-1-1: 2005. Eurocode 3 – design of steel structures – Part 1-1: general rules and rules
7 for buildings; May 2005.
- 8 [33] Amadio C, Bedon C (2013). A buckling verification approach for monolithic and laminated glass
9 elements under combined in-plane compression and bending. *Engineering Structures* 52: 220-229.

List of Tables

Table 1

Table 1. Correction factor k_l for LU beams in LTB [34].

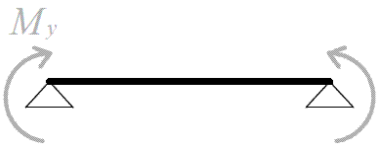
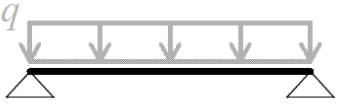

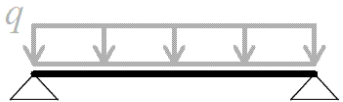
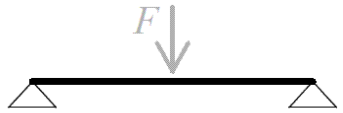
Loading case	Loading condition	Moment distribution	Correction factor k_l
(a)		Constant	1
(b)		Parabolic	1.13
(c)		Triangular	1.32

Table 2

Table 2. Correction factors $k_{l,min}^*$ for LR glass beams in LTB (with $k_y = 0.184\text{N/mm}^2$ the joint stiffness) [5].

Loading case	Loading condition	Load application	Correction factor $k_{l,min}^*$
(a)		Top-edge	0.95
(b)		Bottom-edge	0.95
(c)		Top-edge	0.75
(d)		Bottom-edge	0.85

List of Figures

Figure 1

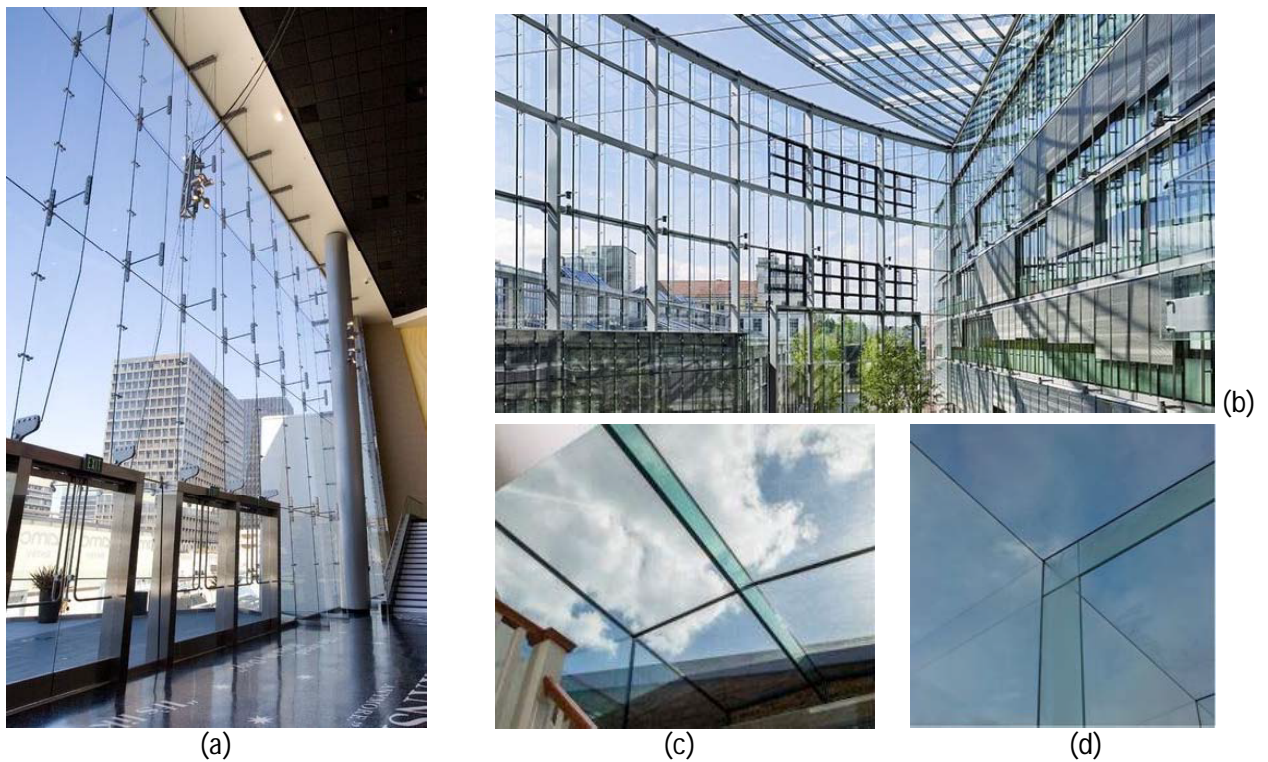


Fig.1. Example of application of glass fins as support for façade panels and roofs.
(a) [1]; (b) [2]; (c) [3]; (d) [4].

Figure 2

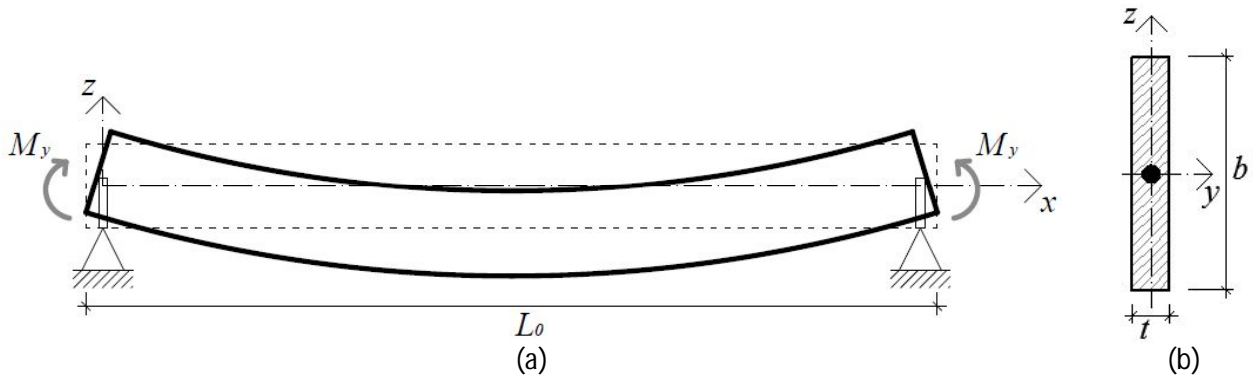


Fig. 2. (a) LTB of a laterally unrestrained monolithic beam under constant bending moment M_y ; (b) cross-section.

Figure 3

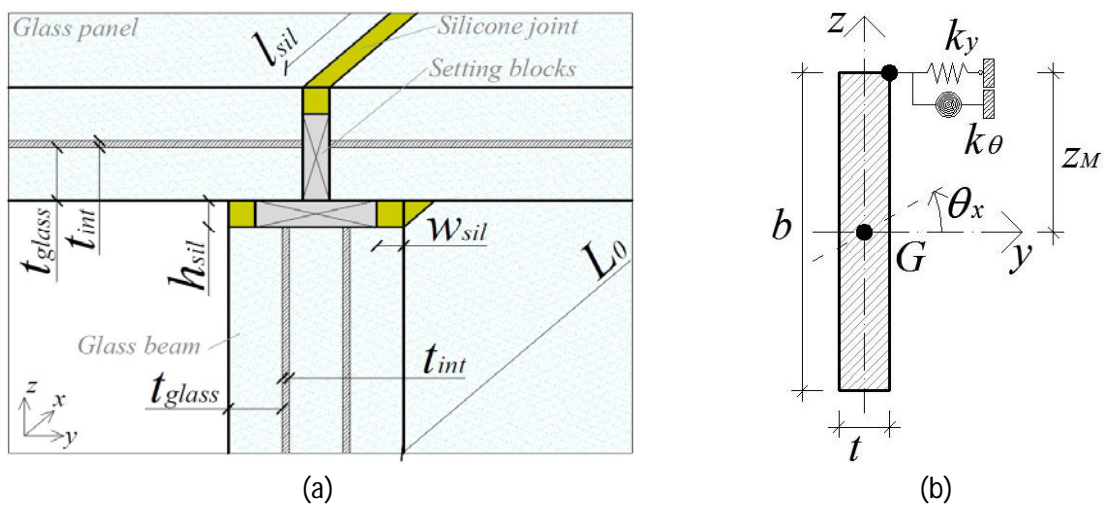


Fig. 3. Typical glass beam-to-roof connection by means continuous silicone joints. (a) Overview and (b) Analytical model (cross-section).

Figure 4

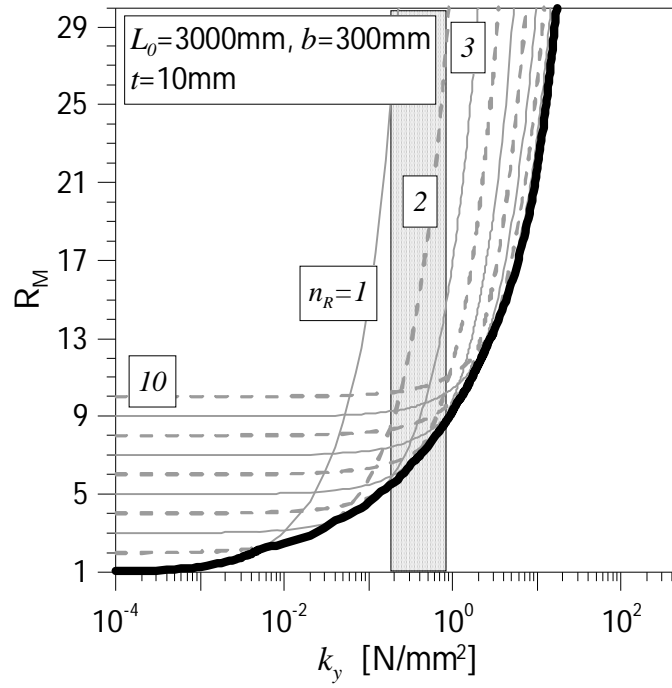


Fig.4. Analytical estimation of the non-dimensional R_M coefficient (Eq.(4)) for a monolithic glass beam under positive, constant bending moment M_y .

Figure 5

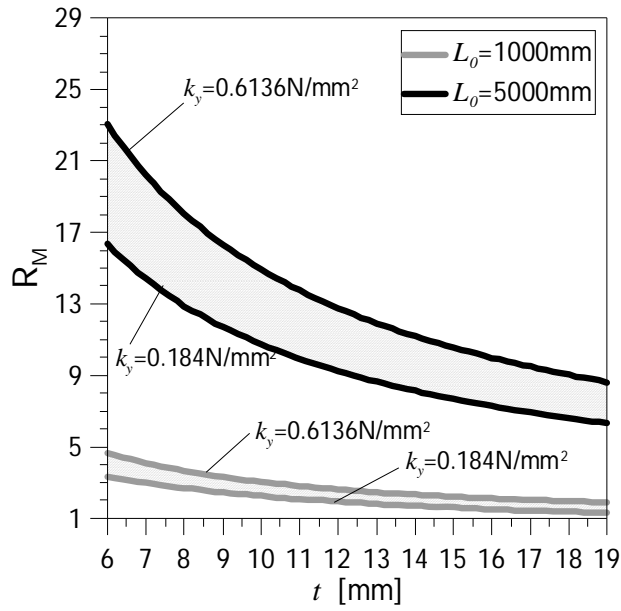


Fig.5. R_M coefficient (Eq.(4)) for LR monolithic glass beams (with $0.184\text{N/mm}^2 \leq k_y \leq 0.6136\text{N/mm}^2$ derived from [5, 27, 29, 30], $k_{\theta} = 0$ and $b = 100\text{mm}$).

Figure 6

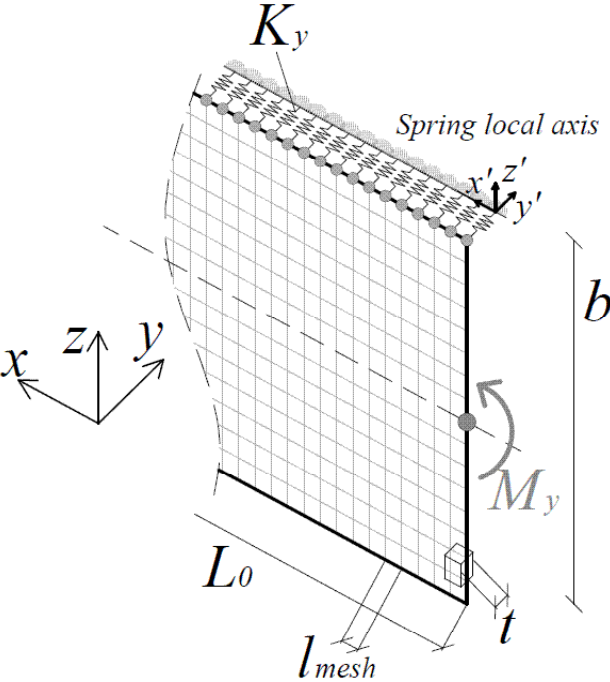


Fig.6. Preliminary FE-numerical study. Detail of the ABAQUS/Standard FE-model.

Figure 7

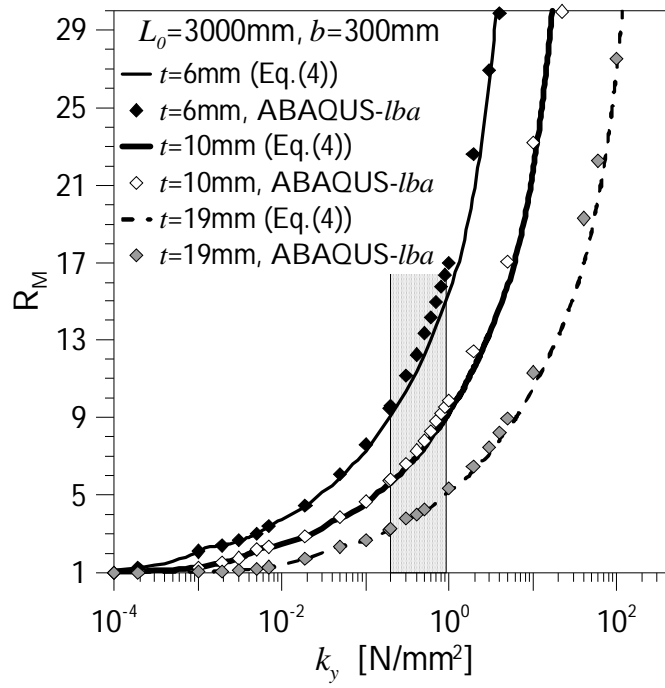


Fig.7. Analytical (Eq.(4)) and numerical (ABAQUS-*lba*) comparison of R_M amplification factors ($k_\theta = 0$).

Figure 8

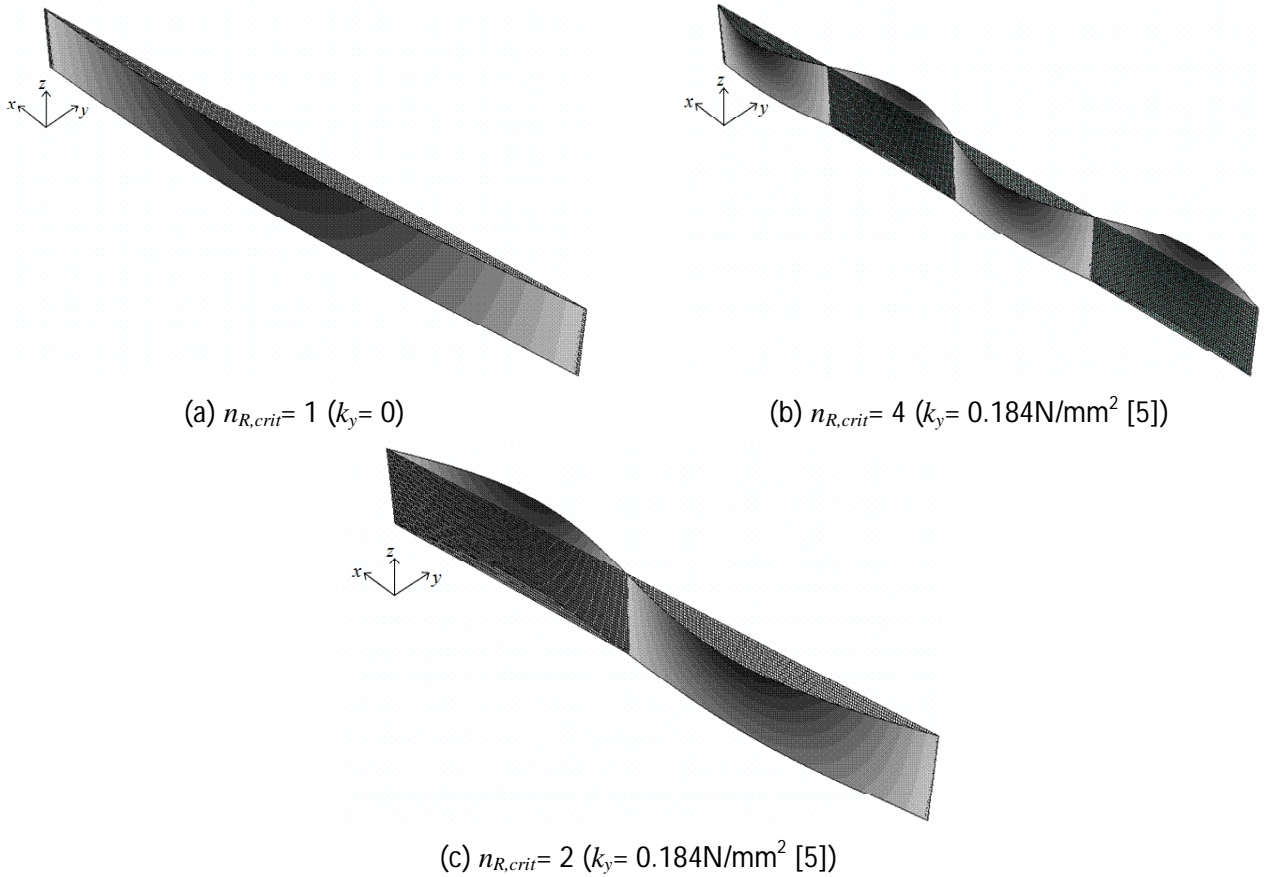


Fig.8. Critical buckling shapes of (a) LU glass beams, compared to (b), (c) LR glass beams. (a) and (b) $L_0 = 3000 \text{ mm}$, $b = 300 \text{ mm}$, $t = 10 \text{ mm}$; (c) $L_0 = 3000 \text{ mm}$, $b = 400 \text{ mm}$, $t = 25 \text{ mm}$. ABAQUS/Standard, white-to-black contour plot.

Figure 9

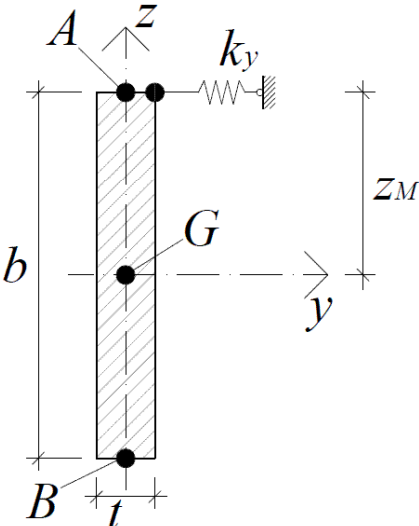


Fig.9. Reference analytical model for the LTB analysis of LR beams under uniformly distributed loads q or concentrated loads F at mid-span.

Figure 10

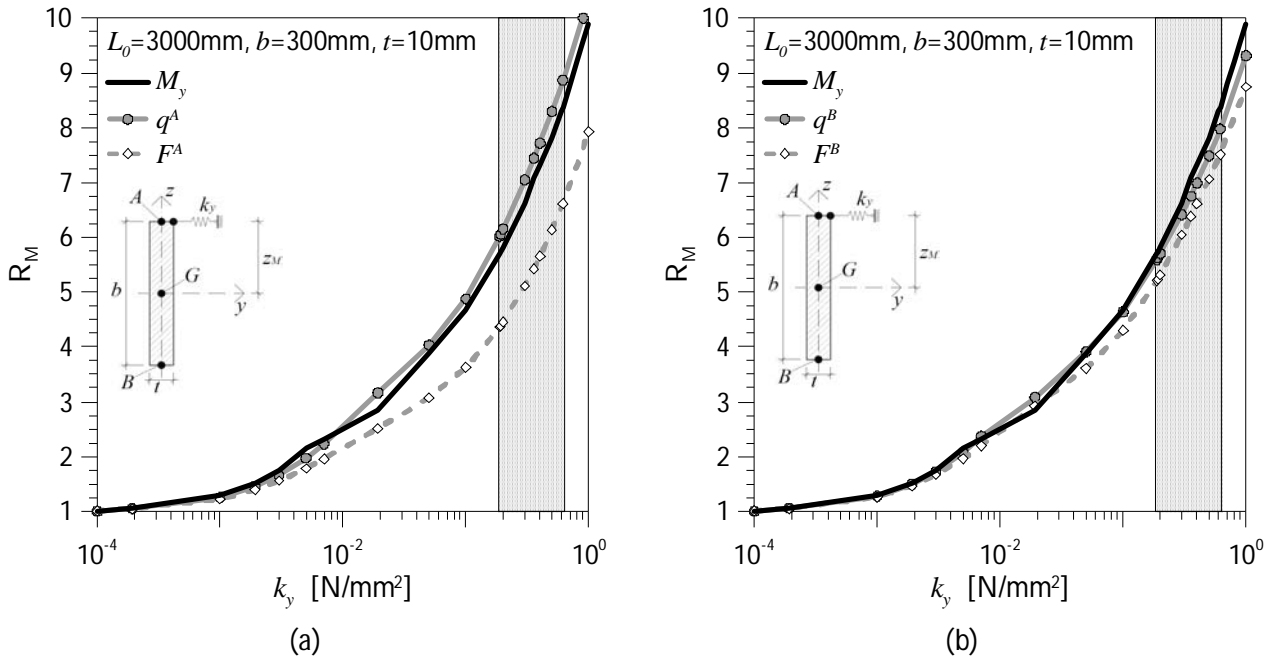


Fig.10. Numerically estimated amplification factor R_M (ABAQUS-*Iba*) for beams under constant bending moment M_y , distributed load q or mid-span concentrated load F . (a) top-edge loads; (b) bottom-edge loads.

Figure 11

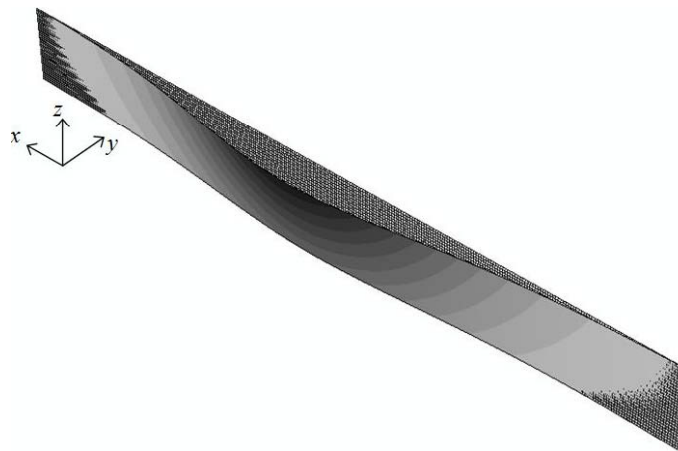


Fig.11. Critical buckling shape of a LR glass beams ($L_0= 3000\text{mm}$, $b= 300\text{mm}$, $t= 10\text{mm}$, with $k_y= 0.184\text{N/mm}^2$ [7]) under top-edge mid-span loads F^A . ABAQUS/Standard, white-to-black contour plot.

Figure 12

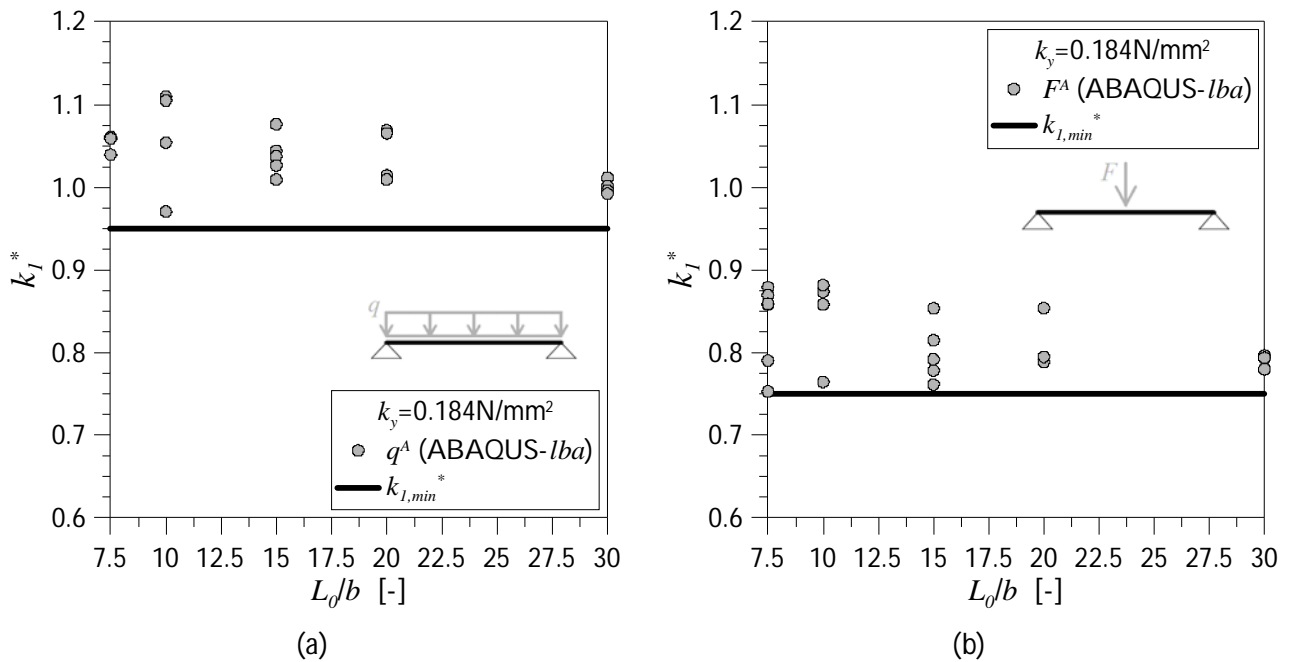


Fig.12. Numerically estimated k_l^* correction factors for LR beams in LTB, with $k_y=0.184\text{N/mm}^2$ the joint stiffness ($1000\text{mm} \leq L_0 \leq 5000\text{mm}$; $8\text{mm} \leq t \leq 25\text{mm}$).
 (a) distributed loads q^A ; (b) mid-span concentrated loads F^A .
 Loads applied at the top-edge of the beams.

Figure 13

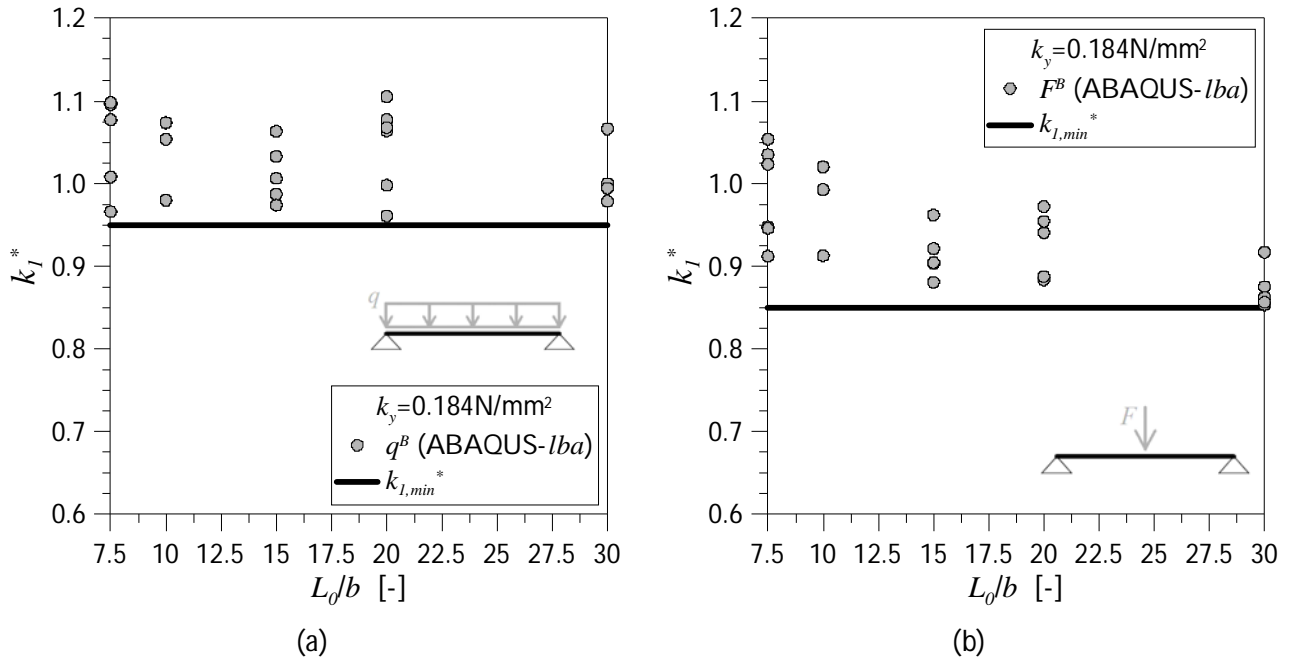


Fig.13. Numerically estimated k_l^* correction factors for LR beams in LTB, with $k_y = 0.184 \text{ N/mm}^2$ the joint stiffness ($1000 \text{ mm} \leq L_0 \leq 5000 \text{ mm}$; $8 \text{ mm} \leq t \leq 25 \text{ mm}$).
 (a) distributed loads q^B ; (b) mid-span concentrated loads F^B .
 Loads applied at the bottom-edge of the beams.

Figure 14

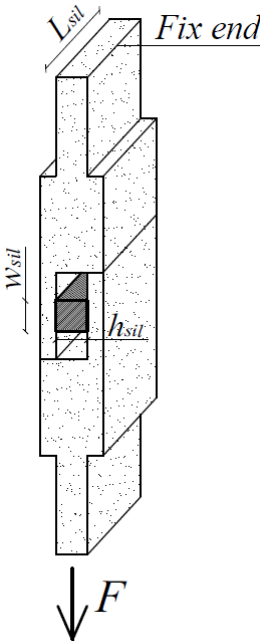


Fig.14. Test setup for shear experiments on silicone sealant joints [6, 7].

Figure 15

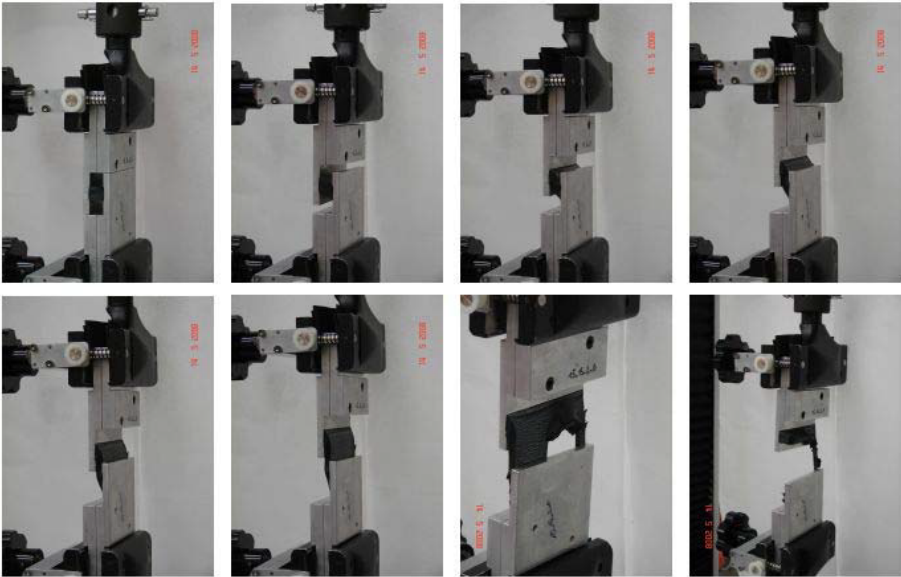


Fig.15. Progressive shear failure of a structural silicone specimen [6, 7].

Figure 16

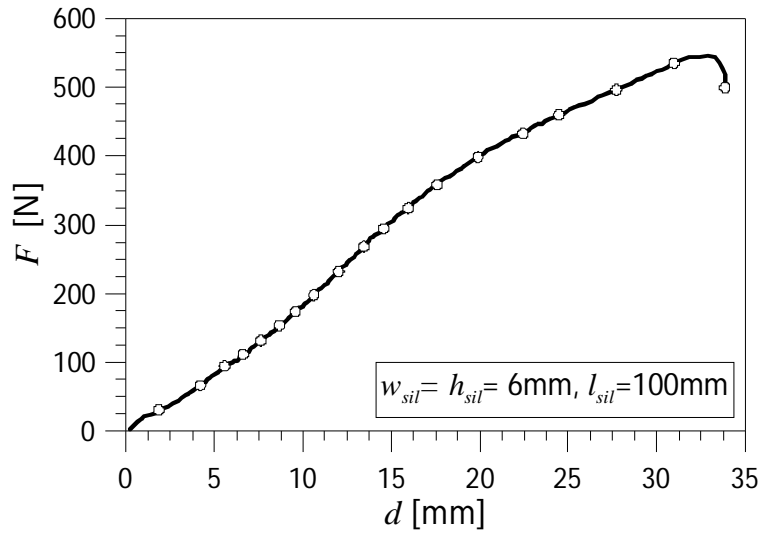


Fig.16. Typical load F – displacement u curve obtained from experiments [6].

Figure 17

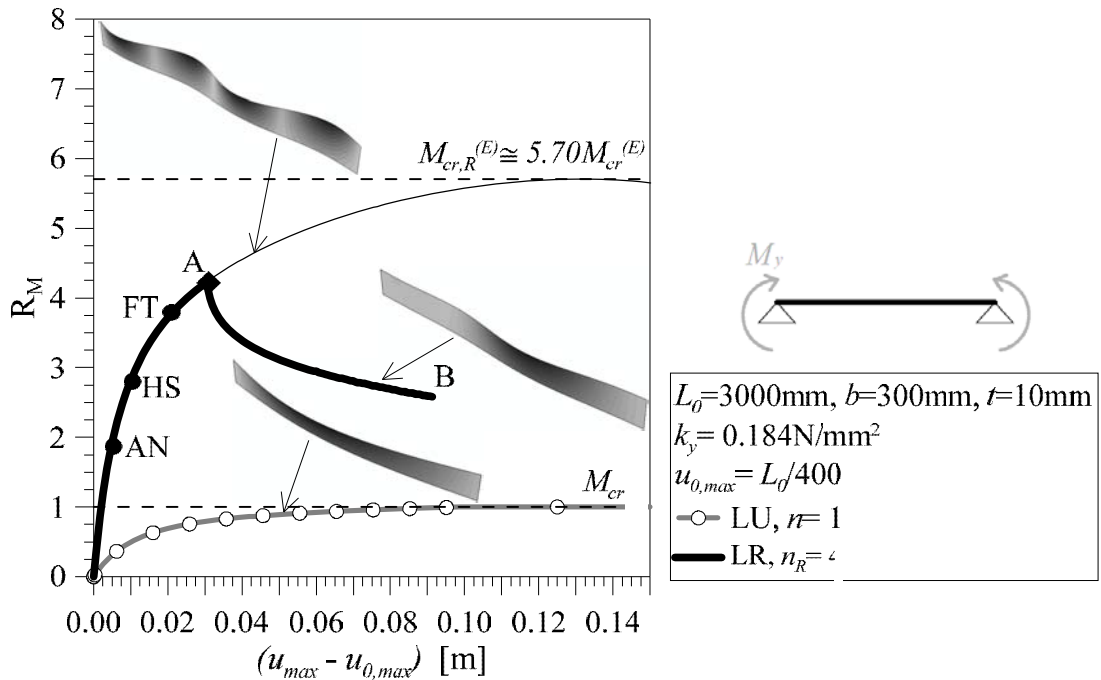


Fig.17. LTB response of a monolithic glass beam laterally unrestrained (LU, $n = 1$) or restrained (LR, $n_R = 4$). Effects of continuous lateral restraints (ABAQUS-*inl*).

Figure 18

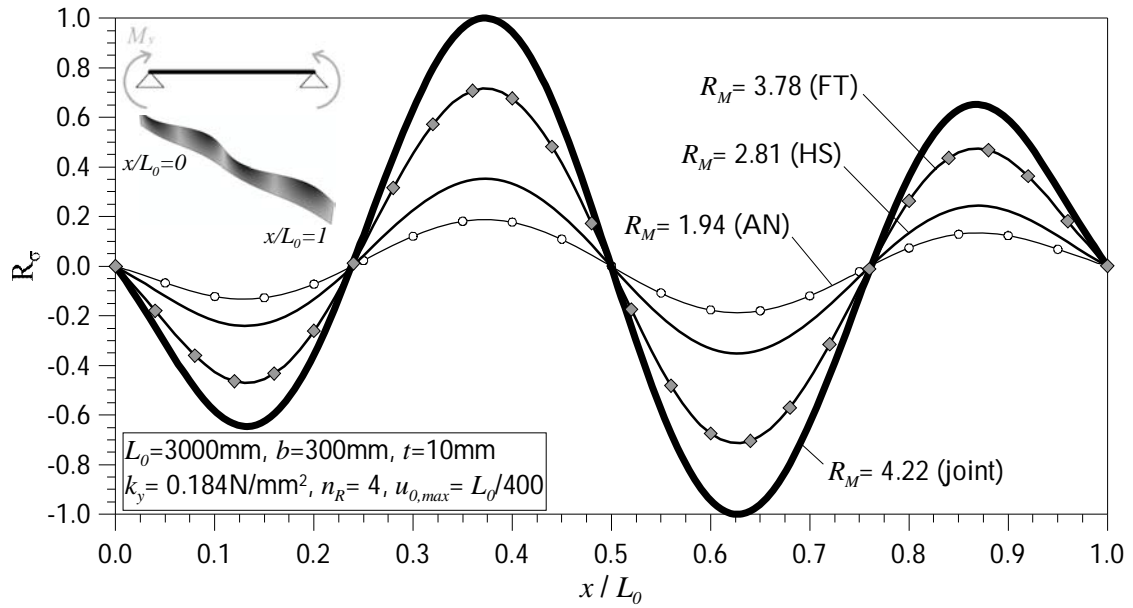


Fig.18. Stress ratio R_{σ} evolution in the silicone joint, as a function of the applied bending moment (ABAQUS-*inl*).

Figure 19

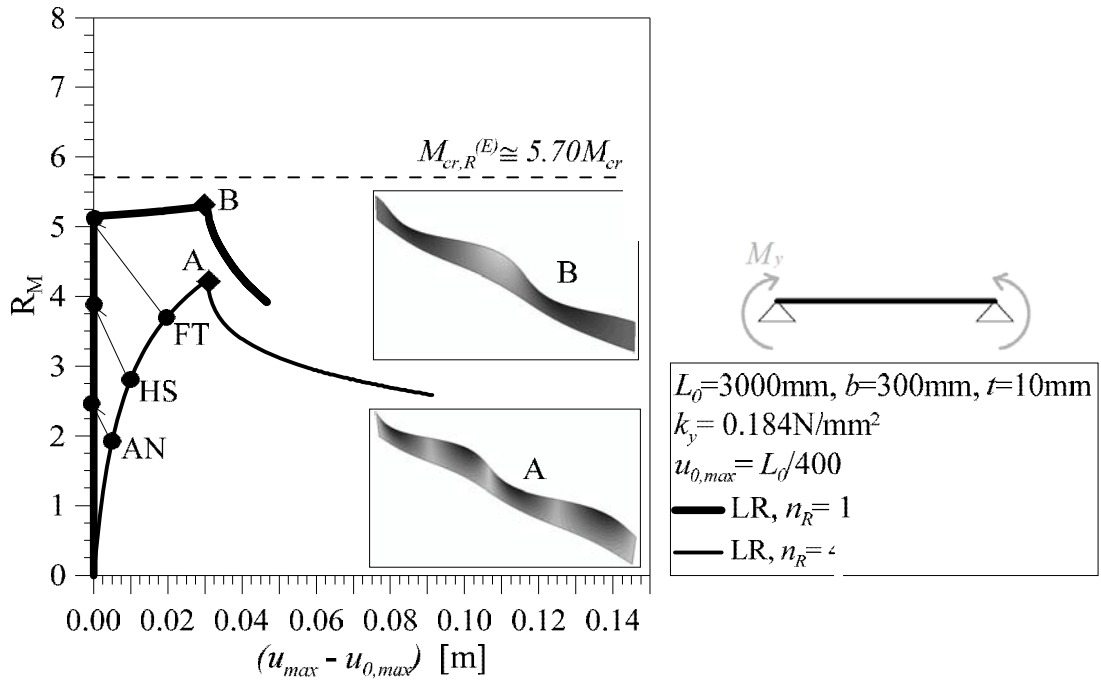


Fig.19. LTB response of a LR monolithic glass beam. Effects of imperfection shape and glass type (ABAQUS-*inl*).

Figure 20

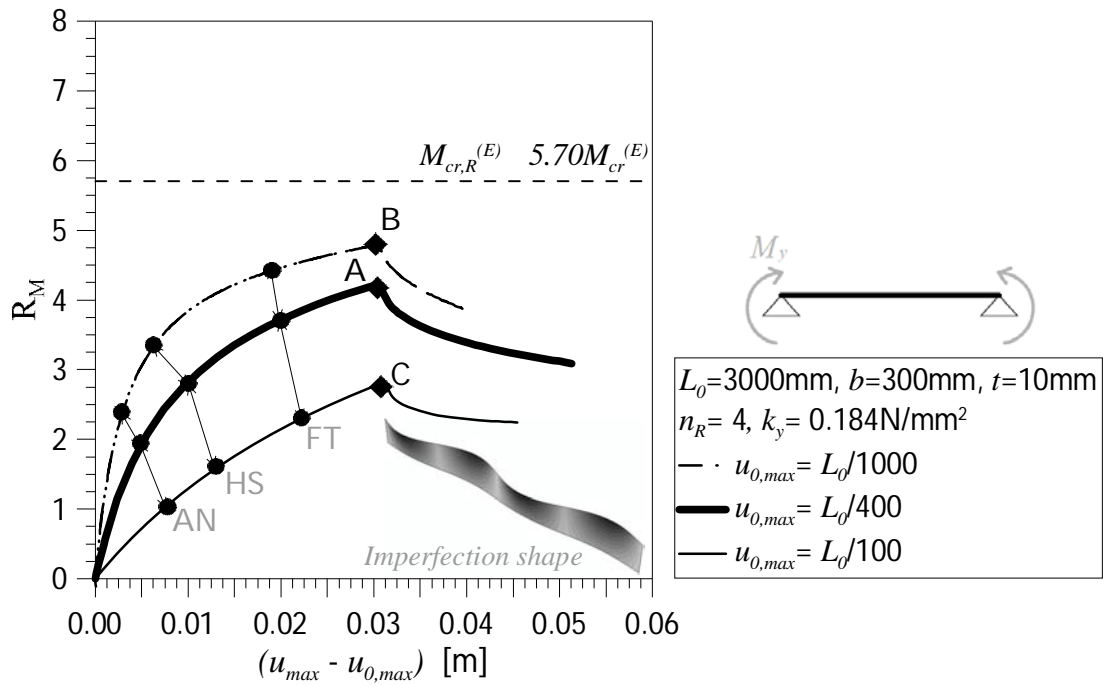


Fig.20. LTB response of a LR monolithic glass beam. Effects of imperfection amplitude and glass type (ABAQUS-intl).

Figure 21

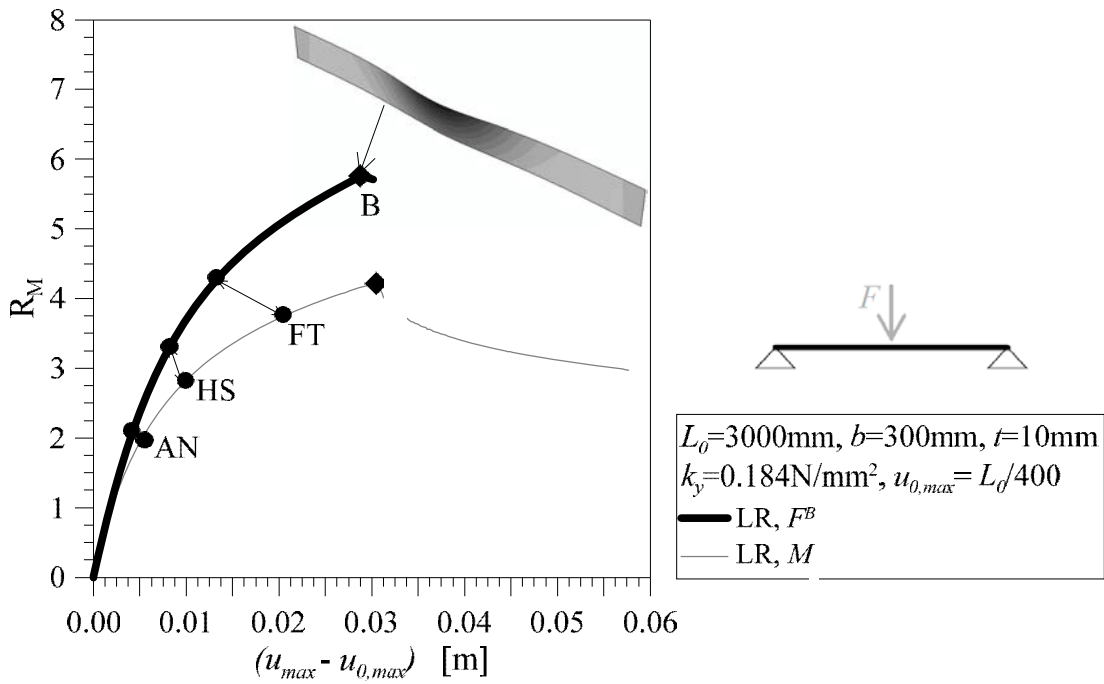


Fig.21. LTB response of a LR monolithic glass beam. Effects of loading condition, with F^B denoting mid-span bottom-edge concentrated loads (ABAQUS-intl).

Figure 22

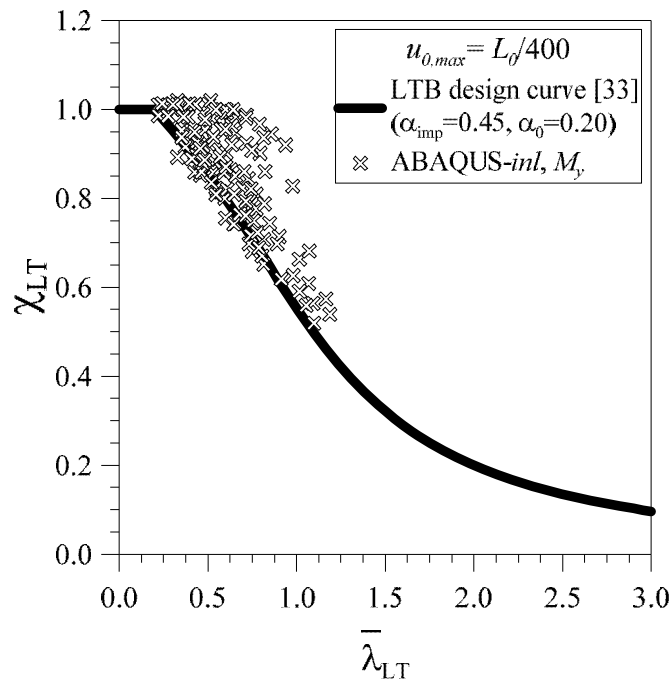


Fig.22. Design buckling curve for LR glass beams in LTB under constant bending moment M_y .

Figure 23

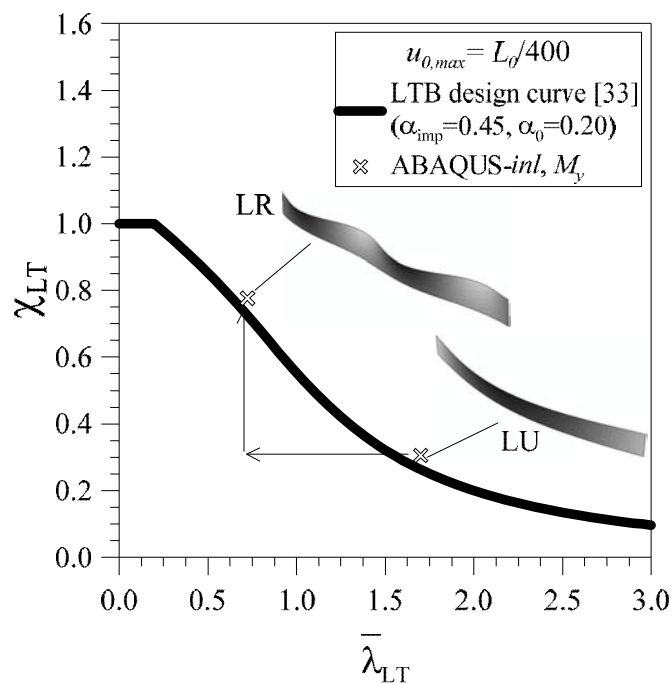


Fig.23. Design buckling curve for glass beams in LTB under constant bending moment M_y . Calculation example for a same beam geometry laterally unrestrained (LU) or continuously restrained (LR) by means of silicone joints.

Figure 24

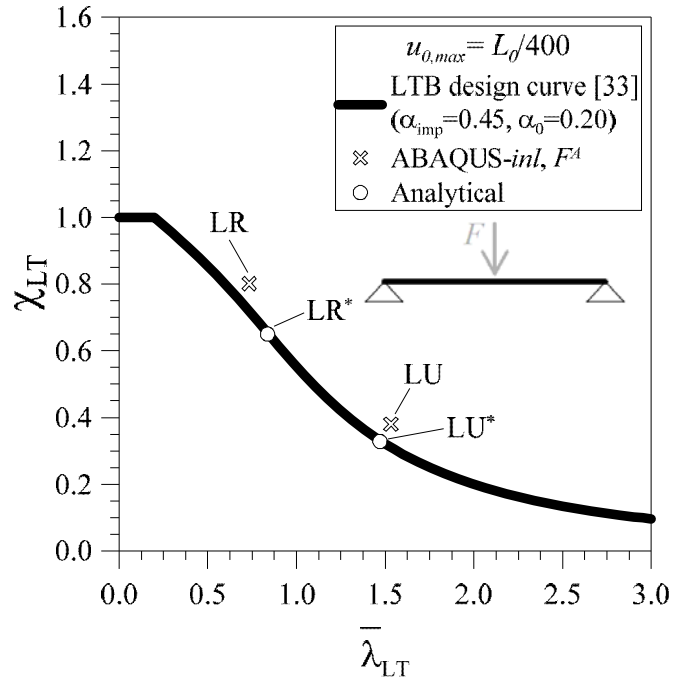


Fig.24. Design buckling curve for glass beams in LTB. Calculation example for a same beam geometry laterally unrestrained (LU) or continuously restrained (LR) by means of silicone joints, subjected to top-edge mid-span concentrated loads F^A .